Strikingly different neurotransmitter release strategies in dopaminergic subclasses

Ana Dorrego-Rivas[1*#], Darren J. Byrne[1*], Yunyi Liu[1], Menghon Cheah[1], Ceren Arslan[1], Marcela Lipovsek[1,2], Marc C. Ford[1], and Matthew S. Grubb[1#]

[1]Centre for Developmental Neurobiology, Institute of Psychiatry, Psychology and Neuroscience (IoPPN), King's College London, London, UK

[2]Current address: Ear Institute, University College London, London, UK

*These authors contributed equally to this work

[#]Corresponding authors: ana.dorrego-rivas@kcl.ac.uk , matthew.grubb@kcl.ac.uk

Abstract

Neuronal function is intimately tied to axodendritic polarity. Neurotransmitter release, for example, is usually the role of the axon. There are widespread exceptions to this rule, however, including many mammalian neuronal types that can release neurotransmitter from their dendrites. In the mouse olfactory bulb, closely related subclasses of dopaminergic interneuron differ markedly in their polarity, with one subtype lacking an axon entirely. These axon-bearing and anaxonic dopaminergic subclasses have distinct developmental profiles and sensory responses, but how their fundamental polarity differences translate to functional outputs remains entirely unknown. Here, we provide anatomical evidence for distinct neurotransmitter release strategies among these closely related dopaminergic subtypes: anaxonic cells release from their dendrites, while axon-bearing neurons release exclusively from their intermittently myelinated axon. These structural differences are linked to a clear functional distinction: anaxonic, but not axon-bearing dopaminergic neurons are capable of self-inhibition. Our findings suggest that variations in polarity can produce striking distinctions in neuronal outputs, and that even closely related neuronal subclasses may play entirely separate roles in sensory information processing.

Introduction

Neurons are one of the most striking examples of cell polarisation. Most neurons have canonical axodendritic polarity, defined by the presence of a somatodendritic domain and a single axon (Banker, 2018). The morphological and molecular specialisation of these distinct compartments gives them unique functional properties, with dendrites usually receiving most synaptic inputs, and axons sending outputs to other neurons by releasing neurotransmitters. However, exceptions to this neuronal polarity dogma are common. In the mammalian brain, there are neurons – including midbrain dopaminergic cells (Pucak and Grace, 1994; Falkenburger et al., 2001) and cortical bitufted cells (Zilberter et al., 1999) – that release neurotransmitter from their dendrites. There are also neurons – including retinal amacrine cells (Wu et al., 2011; Goaillard et al., 2020) – that lack

canonical axons altogether. A remarkable hub for such unconventional neuronal polarity is the olfactory bulb (OB), the first part of the brain that processes information about the sense of smell. Dendritic release of neurotransmitters is a widespread phenomenon in the OB, even in projection neurons and other cells with classically defined axodendritic polarity (Schoppa and Urban, 2003; Hayar et al., 2004; Imamura et al., 2020). In addition, non-canonical polarity is extremely common in the OB, where almost all GABAergic interneurons lack an axon entirely (Tufo et al., 2022).

Neuronal polarity in the OB can be completely different even in closely related neuronal subtypes. In the glomerular layer, a major class of interneurons – around 90,000 cells total in the mouse OB (McLean and Shipley, 1988; Panzanelli et al., 2007; Parrish-Aungst et al., 2007) – releases both dopamine and GABA in order to modulate neurotransmitter release from olfactory sensory neuron terminals and to regulate downstream processing in local circuits (Wachowiak and Cohen, 1999; Berkowicz and Trombley, 2000; Borisovska et al., 2013, Liu et al., 2013; Banerjee et al., 2015; Vaaga et al., 2017; Garg et al., 2025). We recently found that these dopaminergic (DA) neurons can be classified into two subtypes depending on a binary morphological distinction: the presence or absence of an axon. This fundamental divergence in polarity in anaxonic and axon-bearing DA cells is correlated with different excitability profiles and odour response properties (Chand et al., 2015; Galliano et al., 2018; Lau et al., 2024). It also corresponds closely to previous descriptions of OB DA heterogeneity based on cell size (Kosaka and Kosaka, 2008; Pignatelli and Belluzzi, 2017), with axon-bearing DA neurons having significantly larger somas (Kosaka and Kosaka, 2008; Galliano et al., 2018). Whilst axon-bearing DA neurons represent the minority in terms of numbers, making up ~2.5 % of the OB's DA population (Galliano et al., 2018), they have the potential to significantly influence olfactory processing via inter-glomerular inhibition (Kosaka & Kosaka, 2008; Liu et al., 2013; Whitesell et al., 2013; Banerjee et al., 2015). However, the specific function of these two neuron subtypes within OB glomerular networks is not fully understood. A crucial outstanding question is how the structural differences in these two neuron subtypes translate into strategies for influencing bulbar circuits via neurotransmitter release.

Anaxonic DA neurons only have a soma and dendrites (Chand et al., 2015; Galliano et al., 2018) making these the sole available domains for neurotransmitter release. Indeed, dendritic presynaptic structures are present in DA neurons (Kiyokage et al., 2017), and are associated with these cells' functional ability to self-inhibit via local GABA release (Smith and Jahr, 2002; Murphy et al., 2005; Maher and Westbrook, 2008). On the other hand, axon-bearing DA neurons are known to be the sole source of long-range interglomerular connections in the OB (Kosaka and Kosaka, 2008), with functional studies showing that these cells release neurotransmitters over these long-distance axonal projections (Liu et al., 2013; Whitesell et al., 2013; Banerjee et al., 2015). However, in a brain region where dendritic release is the norm rather than the exception, what remains unknown is whether axon-bearing DAs combine this distal, *inter*glomerular signalling with local, *intra*glomerular inhibition via release from their dendrites. Answering this question has important implications for how information is processed in early olfactory circuits.

Here, we provide anatomical evidence showing that axon-bearing OB DA neurons have axons with neurotransmitter release sites, while their dendrites lack these sites almost entirely. On the other hand, we found that all anaxonic DA neurons have release sites on their dendrites. These structural differences are associated with a striking functional distinction: while all anaxonic neurons can self-inhibit, there is an almost total absence of self-inhibition responses in the axon-bearing subpopulation. This polarity-based dichotomy suggests that even these closely related interneuron subtypes may play entirely separate roles in the processing of sensory information.

Results

Labelling putative presynaptic structures in individual olfactory bulb dopaminergic neurons

We first developed a structural approach for labelling putative presynaptic sites in individual OB DA neurons. We observed that synaptophysin, a membrane protein located in vesicles at the presynapse, is expressed in OB DA cells at both the mRNA (**Figure 1A**) and protein (**Figure 1B**) levels. Given the high synaptic density and complexity of OB glomeruli, it is not possible to reliably assign specific synaptophysin label to individual DA neurons using widespread staining of endogenous protein. We therefore chose a sparse labelling approach based on the injection of an AAV-DJ-hSyn-FLEx-mGFP-T2A-Synaptophysin-mRuby construct (Beier et al., 2015; Kathe, et al., 2022). This vector allows the expression in individual cre-expressing cells of a membrane-bound GFP for cell morphology, and fluorophore-tagged full-length synaptophysin for the visualisation of putative presynaptic puncta. There is strong evidence showing that the overexpression of fluorophore-tagged synaptophysin is functionally benign (Granseth et al., 2006; Li and Tsien, 2012).

We performed *in utero* injections in embryonic day 14 (E14) vGAT (vesicular GABA transporter)-cre mice. Since OB dopaminergic neurons are also GABAergic (Kosaka and Kosaka 2008; 2016; Maher & Westbrook 2008; Borisovska et al., 2013; Vaaga et al., 2016; Liu et al. 2013) and express vGAT at both the mRNA (**Figure 1A**) and protein (**Figure 1B**; Panzanelli et al., 2007) levels, this conditional line gives access to both anaxonic and axon-bearing DA subclasses, alongside many non-dopaminergic OB GABA-releasing neurons (Galliano et al., 2018). Dopaminergic neurons were then specifically identified via immunostaining against tyrosine hydroxylase (TH). TH is the rate-limiting enzyme in catecholamine synthesis and, because of the absence of noradrenergic neurons in the OB, is a specific and comprehensive marker for all dopaminergic cells in this brain region (Hokfelt et al., 1975; Rosser et al., 1986; Kosaka and Kosaka 2016; Galliano et al., 2018).

We chose an embryonic timepoint for viral targeting to ensure the effective and sparse labelling of axon-bearing and anaxonic DA neurons (**Figure 1C**). Early infection before cells have migrated to their final positions produced sparse labelling which, when analysed in juvenile postnatal animals, permitted the unambiguous identification of an individual neuron's processes. Embryonic targeting also had the benefit of equally sampling DA subclasses. While anaxonic DA neurons are born throughout life, axon-bearing DA cells are exclusively generated in embryonic development (Batista-Brito et al., 2008; Galliano et al., 2018). Embryonic injections therefore ensured effective and more balanced labelling of both populations.

We were able to detect well-defined synaptophysin-mRuby puncta along the processes of TH+ GFP+ neurons (**Figure 1D**). To assess whether this method labels reliable presynaptic release sites in DA neurons, we co-stained the injected tissue against vGAT and observed high co-localisation between endogenous vGAT and mRuby label (**Figure 1E**; 39/53 = 74 % synaptophysin-mRuby puncta co-localised with vGAT; n = 9 cells from N = 4 mice). These results demonstrate that a large proportion of synaptophysin-mRuby puncta are likely to reflect putative presynaptic release sites in OB DA neurons.

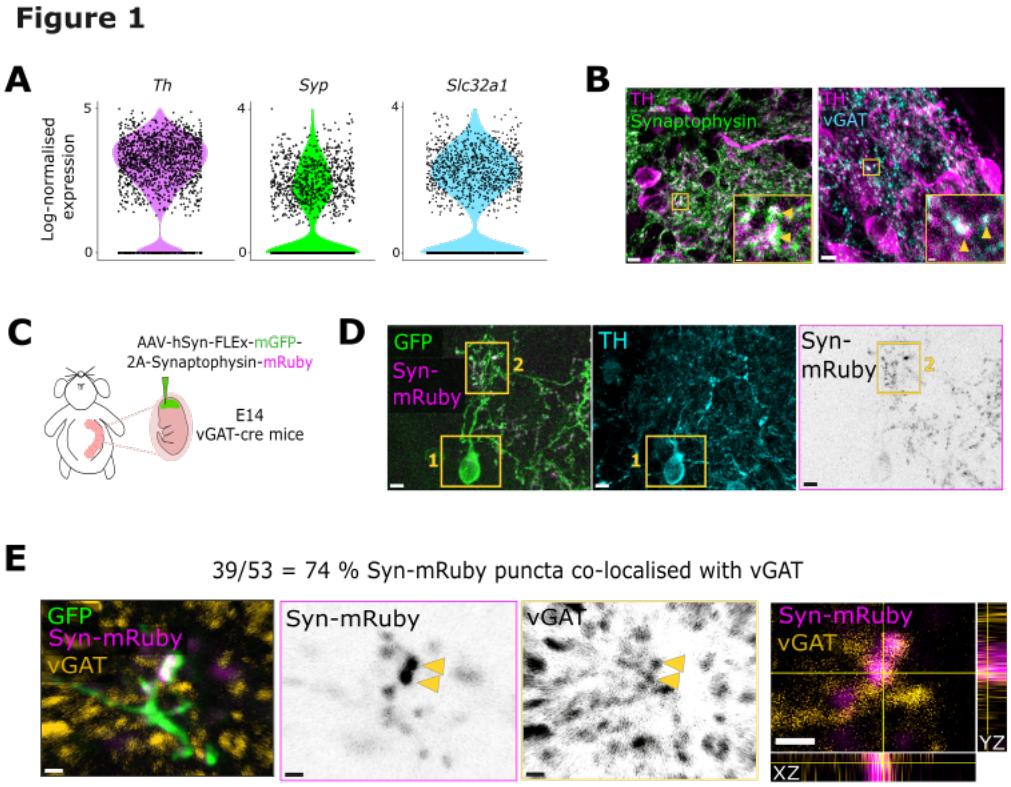

Figure 1. **Labelling putative presynaptic structures in individual olfactory bulb dopaminergic neurons. (A)** Log_2-normalised expression of *Th* (tyrosine hydroxylase), *Syp* (Synaptophysin) and *Slc32a1* (vGAT) mRNA in DA neurons from single cell RNA sequencing data (Brann et al., 2020). **(B)** Example confocal images of endogenous immunostaining for synaptophysin (green) and TH (magenta) on the left, and vGAT (blue) and TH (magenta) on the right. Both images were taken in the glomerular layer of the OB. Yellow arrowheads point to small clusters where TH and synaptophysin or TH and vGAT co-localise. Scalebars: 5 µm (main) and 0.5 µm (inset) for the images on the left, 4 µm (main) and 1 µm (inset) for the images on the right. **(C)** Strategy to label putative presynaptic release sites in individual DA neurons. **(D)** Example confocal image of a successfully labelled DA cell. Inset 1 reveals the TH+ dopaminergic identity of the neuron (cyan) and inset 2 highlights the Syn-mRuby puncta (magenta, black). Scalebars, 5 µm. **(E)** Example confocal image of a GFP+ (green), Syn-mRuby+ (magenta, black) neuronal process co-stained with vGAT (orange, black). Yellow arrowheads indicate examples where Syn-mRuby and vGAT puncta co-localise. The last panel shows the orthogonal views of the bottom punctum. Scalebars, 1 µm.

151 **Anaxonic DA neurons have dendritic neurotransmitter release sites**

152 Given that anaxonic DA neurons lack an axon, and are known to release both GABA and dopamine,
153 to be able to release neurotransmitter they must have presynaptic release sites on their dendrites.
154 We identified this neuronal subtype in our population of GFP+/TH+ neurons by the lack of the
155 proximal axonal marker TRIM46 (**Figure 2A**, van Beuningen et al., 2015; Galliano et al., 2018).

Figure 2

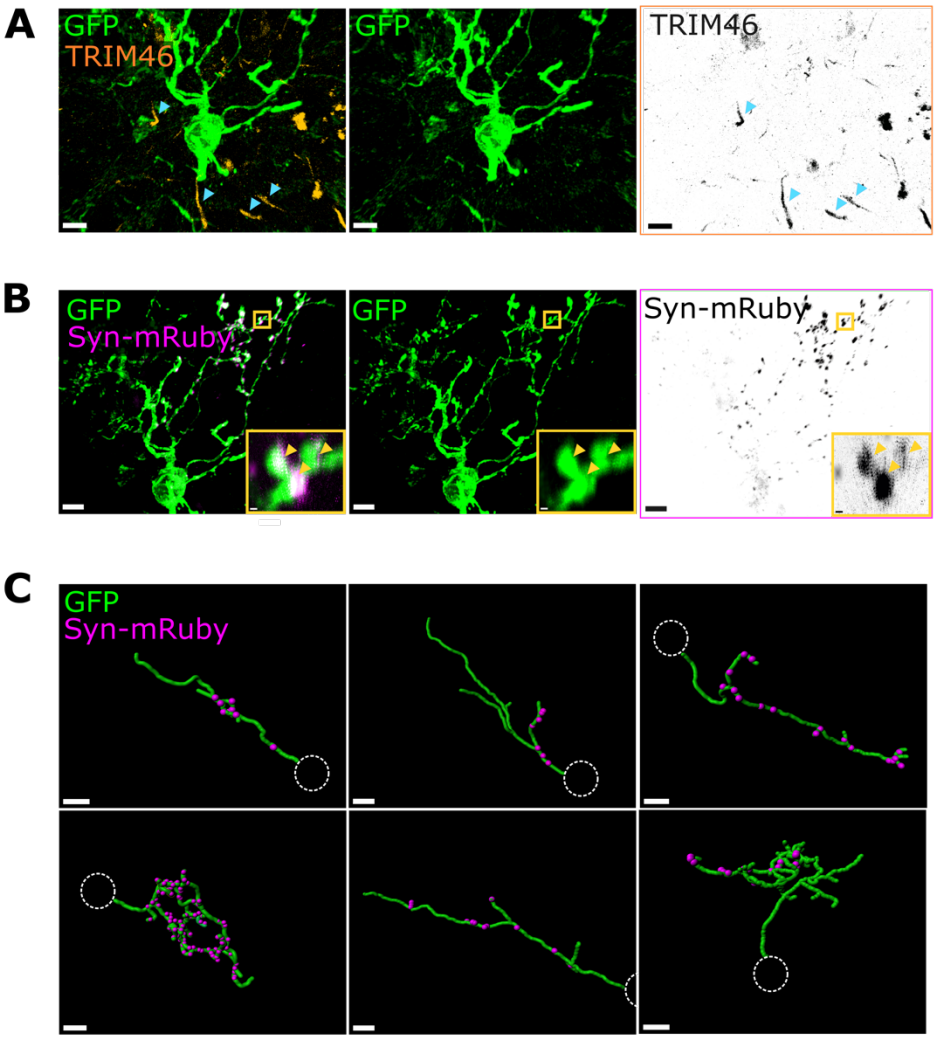

156 **Figure 2**. **Anaxonic DA neurons have dendritic neurotransmitter release sites. (A)** Example confocal image of
157 a TRIM46-negative anaxonic DA neuron. Blue arrowheads point to examples of other TRIM46+ AISs (orange,
158 black) in the same region which do not co-localise with this neuron's GFP signal. Scalebars, 5 μm. **(B)** Snapshot
159 of the same neuron in (A) showing Synaptophysin-mRuby Puncta (magenta, black) on the dendrites. Yellow
160 inset highlights a region of the neuron with multiple mRuby+ puncta within the GFP+ (green) processes (yellow
161 arrows). Scalebars, 5 μm and 0.5 μm. **(C)** Example snapshots from 3D dendritic reconstructions (green, GFP)
162 and presynaptic puncta detection (magenta, Syn-mRuby) of anaxonic DA neurons. Note: these are not full
163 dendritic reconstructions, but example dendrites. Dotted white circle represents the soma location. Scalebars,
164 5 μm.

165

166 As predicted, we found that all anaxonic neurons had synaptophysin-mRuby puncta in their
167 dendrites (**Figure 2B, C;** n=9 anaxonic DA cells from N=4 mice). The thin slices necessary for puncta
168 detection precluded any comprehensive analysis of dendritic morphology or synaptic distributions.
169 The resultant sub-sampling of individual cells' arbours may also have contributed to the variability in
170 puncta density we observed across neurons (**Figure 2C**), although similarly high variability between
171 OB dopaminergic cell presynaptic specialisations has been shown in previous ultrastructural analyses
172 (Kiyokage et al., 2017). We saw no consistent evidence for spatial patterns, clusters, or privileged
173 branches; instead, puncta were distributed throughout each cell's dendritic arbour (**Figure 2C**).
174 These results provide anatomical evidence for the presence of dendritic neurotransmitter release
175 sites in anaxonic DA neurons.

176

177 **Axon-bearing DA neurons have release sites on their intermittently myelinated axons, but not on**
178 **their dendrites**

179 Long-range GABA release has been functionally demonstrated in dopaminergic neurons (Liu et al.,
180 2013; Whitesell et al., 2013; Banerjee et al., 2015), strongly suggesting that axon-bearing DA neurons
181 have axonal release sites. It was not possible to follow TRIM46+ DA axons for long distances from
182 the soma in thin brain slices, so instead we used the distal axon marker myelin basic protein (MBP).
183 In the first description of myelination in this cell type, we found that DA axons are myelinated in an
184 intermittent pattern, a common trait in other brain regions (**Figure 3A**, Tomassy et al., 2014). Using
185 MBP as indicator of axon identity, we were then able to locate synaptophysin-mRuby puncta in
186 unmyelinated sections of GFP+ TH+ axons (**Figure 3B and Supplementary Figure 1;** n=5 axon-bearing
187 DA cells from N=3 mice). As predicted, axon-bearing DA neurons therefore have putative presynaptic
188 release sites on their axons.

189 Most neurons with canonical axodendritic polarity in the olfactory bulb release neurotransmitters
190 from both axons and dendrites (Castro and Urban, 2009). To assess if this scenario also holds true for
191 DA axon-bearing cells, we explored the dendritic localisation of synaptophysin-mRuby-labelled
192 presynaptic release sites in GFP+ neurons with clear TRIM46+ proximal axonal domains (**Figure 3C**).
193 As expected, these axon-bearing OB DA cells had larger somas than their anaxonic neighbours
194 (**Figure 3D and Supplementary Figure 2A**; soma area: 110.3 ± 7.72 μm^2 for axon-bearing DA cells,
195 61.99 ± 4.41 μm^2 for anaxonic DA neurons; n = 11 axon-bearing cells and n = 9 anaxonic neurons
196 from N = 5 mice; unpaired t-test with Welch's correction, $p < 0.0001$). Given previous findings that
197 axon-bearing DA cells have more widely ramified dendritic trees (Galliano et al., 2018), we ensured
198 that our reconstructions of TRIM46-negative dendritic processes were equally extensive in both cell
199 subtypes (**Supplementary Figure 2B;** maximum length of reconstructed dendrites: 67.64 ± 8.96 μm
200 for axon-bearing DA cells, 74.88 ± 11.68 μm for anaxonic DA neurons; n = 11 axon-bearing cells and
201 n = 9 anaxonic neurons from N = 5 mice; unpaired t-test with Welch's correction, $p = 0.6299$). We
202 found that, unlike their anaxonic counterparts, almost all TRIM46+ neurons (10/11 cells from N = 4
203 mice, = 90.9 %) did not have any synaptophysin-mRuby puncta on their dendrites (**Figure 3E, F**;
204 dendritic puncta density: 0.02 ± 0.02 $(\mu m)^{-1}$ for axon-bearing cells, 0.19 ± 0.04 $(\mu m)^{-1}$ for anaxonic
205 neurons; n = 11 axon-bearing cells and n = 9 anaxonic neurons from N = 5 mice; Mann-Whitney test;
206 $p = 0.0001$). We did find one single axon-bearing DA neuron with apparent dendritic puncta;
207 however, this cell had dramatically higher levels and unusual patterns of expression as compared to
208 all other GFP+ neurons (**Supplementary Figure 2C, D**) and we include it in our sample only through

209 an abundance of caution. These findings provide a structural basis for dendritic neurotransmitter
210 release in anaxonic DA neurons, but not in the axon-bearing population of DA neurons in the OB.

Figure 3

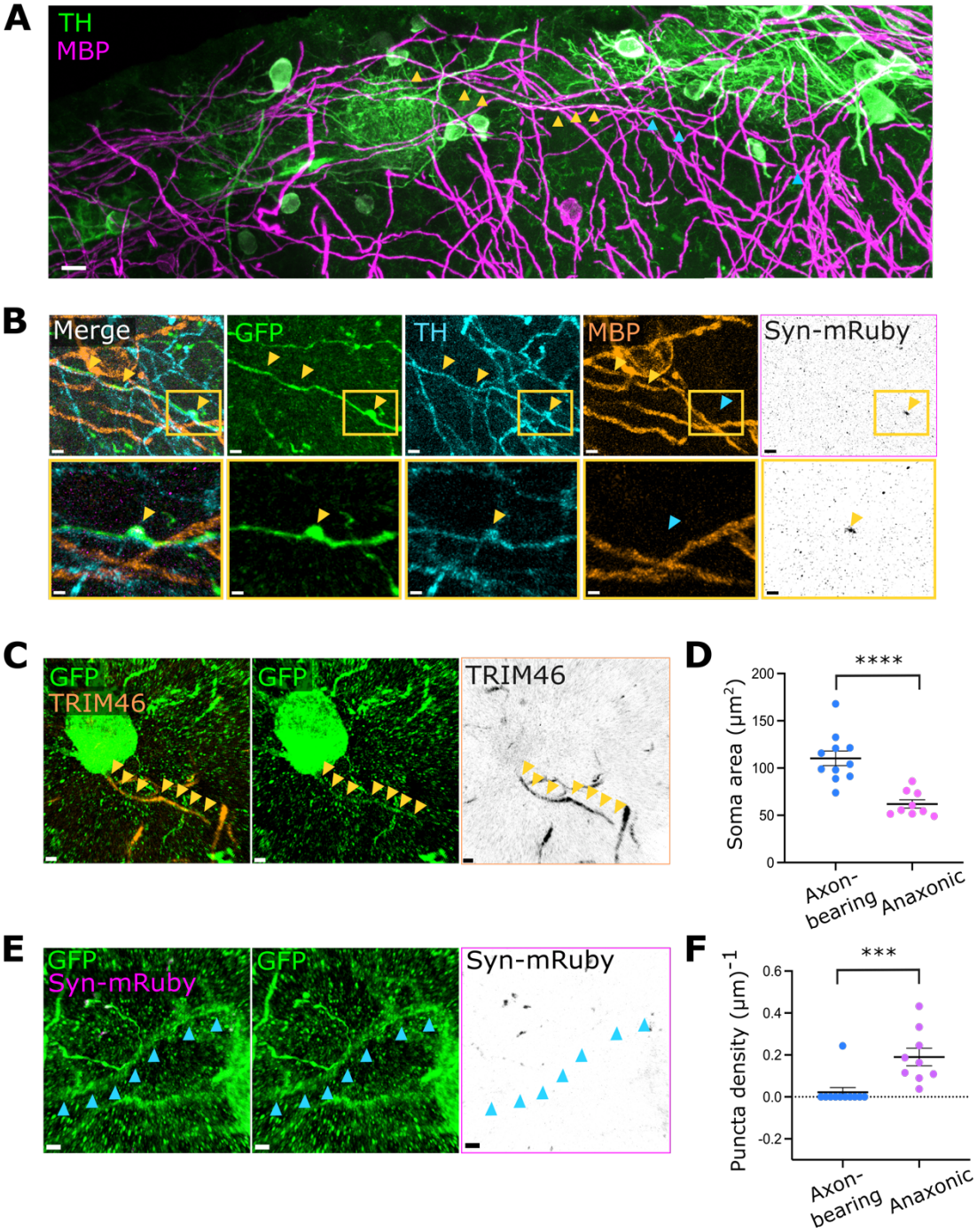

211 **Figure 3**. **Axon-bearing DA neurons have release sites on their intermittently myelinated axons, but not on**
212 **their dendrites. (A)** Stitching of individual confocal stacks processed for maximum intensity projections of OB
213 DA neurons co-stained with TH (green) and myelin basic protein (MBP, magenta). Yellow arrowheads point to
214 myelinated parts of the axon, blue arrowheads show unmyelinated areas. Scalebar, 10 µm. **(B)** Example
215 confocal images of a distal DA axon stained with GFP (green), TH (cyan), MBP (orange) and synaptophysin-
216 mRuby (magenta, black). Yellow inset highlights the location of the presynaptic bouton. Yellow arrowheads

point to co-localised regions, blue arrowheads show non-co-localisation. Scalebars, 2 μm and 1 μm. **(C)** Confocal image of an axon-bearing TRIM46+ DA neuron. Yellow arrowheads show co-localised staining for GFP (green) and TRIM46 (orange, black). Scalebars, 2 μm. **(D)** Soma area of axon-bearing and anaxonic DA neurons. Each dot shows one cell; lines show mean ± SEM; n = 11 axon-bearing cells and n = 9 anaxonic neurons from N = 5 mice; unpaired t-test with Welch's correction; ****, p <0.0001. **(E)** Snapshot of the same axon-bearing DA neuron shown in (C), co-stained with GFP (green) and synaptophysin-mRuby (magenta, black). Blue arrows show dendritic segments lacking mRuby label, despite the presence of clear mRuby+ puncta in neighbouring processes from a different GFP+ cell. Scalebars, 2 μm. **(F)** Dendritic puncta density in axon-bearing and anaxonic DA neurons. All conventions as in D; n = 11 axon-bearing cells and n = 9 anaxonic neurons from N = 5 mice; Mann-Whitney test; **, p = 0.0001.

Anaxonic DA neurons are capable of GABAergic self-inhibition

The fact that dendritic release sites are likely located near dendritic receptors (Kiyokage et al., 2017) might have the functional consequence that anaxonic DA cells can signal to themselves and influence their own activity. We found that OB DA neurons do not express DA receptors at the mRNA level (**Figure 4A**), making it unlikely that they could influence their own activity via DA signalling. However, GABAergic auto-evoked inhibition (AEI) or self-inhibition has been described in OB periglomerular cells in general, and in DA neurons in particular (Smith and Jahr, 2002; Murphy et al., 2005; Maher and Westbrook, 2008; Borisovska et al., 2013).

To address if the anaxonic subtype of DA neuron can self-inhibit, we used the DAT-tdT mouse line to specifically target DA neurons (Bäckman et al., 2006; Madisen et al., 2009; Galliano et al., 2018; Byrne et al., 2022; see Materials and Methods) and performed whole-cell patch clamp recordings in tdT+ cells to evoke AEI responses. We identified the anaxonic DA population by their characteristic 'monophasic' phase-plane plot profile (**Figure 4B**; Galliano et al., 2018). After evoking transmitter release with transient depolarisation, we observed a prolonged inward current which was blocked by adding the GABA-A receptor antagonist gabazine at 10 μM (**Figure 4C;** AEI charge: 44.11 ± 6.02 pC; n = 31 cells from N = 18 mice). These data reveal that anaxonic DA neurons display AEI responses, consistent with the co-existence of presynaptic release sites and postsynaptic targets in the dendrites of these cells.

Although the AEI response is initiated by the depolarisation of the recorded anaxonic DA neuron, it has always been assumed, but not demonstrated, that the response is the direct result of GABA released from the same cell. However, given the presence of other GABAergic cells in local glomerular circuits (Kiyokage et al., 2017; for review see Tufo et al., 2022), there are other potential indirect ways in which depolarising a DA neuron might produce a GABA response in that same cell.

DA neurons in the OB release GABA and dopamine (Borisovska et al., 2013), and D1-like and D2-like dopamine receptors are expressed in the glomerular layer (Coronas et al., 1997). When we depolarise an anaxonic DA neuron to evoke neurotransmitter release, it is therefore possible that the dopamine that is co-released with GABA activates the dopamine receptors of neighbouring neurons, evoking secondary GABA release that then drives the AEI response in the recorded cell (**Figure 4D**). To rule out this possibility, we showed that despite a non-significant trend towards a reduction in charge, the AEI response was still clearly present after the application of D1-like and D2-like receptor antagonists (10 μM SKF 83566-hydrobromide and 10 μM sulpiride, respectively; **Figure 4E, F**; AEI charge before blockers: 25.93 ± 4.99 pC , charge after blockers: 17.37 ± 3.47 pC; n = 6 cells from N = 4 mice; paired t-test, p = 0.21). We also saw no significant alteration in AEI decay kinetics after the application of dopamine receptor antagonists (**Supplementary Figure 3**; decay constant k

before blockers: 0.03 ± 0.003 ms^{-1}; k after blockers: 0.03 ± 0.006 ms^{-1}; n = 6 cells from N = 4 mice; Wilcoxon matched-pairs test, p = 0.84). These results show that the AEI response is not mediated by dopamine acting through other neurons.

Figure 4

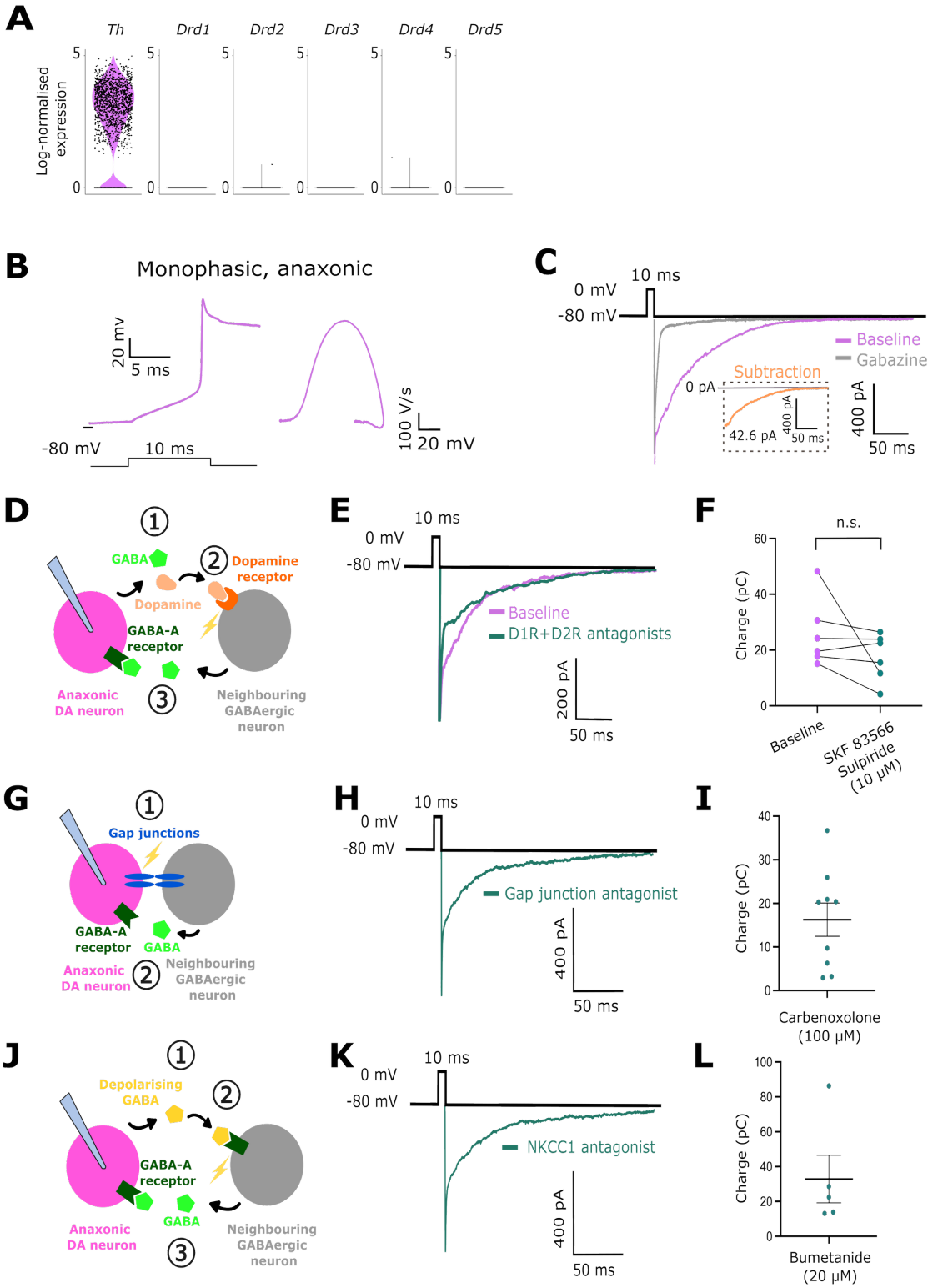

266 **Figure 4**. **Anaxonic DA neurons are capable of self-inhibition. (A)** Log_2-normalised expression of *Th, Drd1,*
267 *Drd2, Drd3, Drd4* and *Drd5* mRNA in OB DA cells. **(B)** Example trace of an action potential fired by a putative
268 anaxonic DA neuron (left) and its monophasic phase-plane plot profile (right). Note the prolonged
269 repolarisation due to Cs-based internal solution. **(C)** Example traces of an AEI response recorded before
270 (magenta) and after (grey) the application of gabazine. The subtraction is shown in the orange inset trace. **(D)**
271 Schematic showing the potential involvement in the AEI response of neighbouring GABAergic neurons
272 activated by dopamine released from the patched DA cell. **(E)** Example traces of an AEI response before
273 (purple) and after (green) applying D1-like and D2-like receptor blockers (hydrobromide and sulpiride, each at
274 10 μM). **(F)** AEI charge before (purple) and after (green) applying dopamine receptor antagonists; n = 6 cells
275 from N = 4 mice; paired t-test, p = 0.21, n.s. = non-significant. **(G)** Schematic showing the potential
276 involvement in the AEI response of neighbouring GABAergic neurons activated via gap junctions. **(H)** Example
277 trace of an AEI response in the presence of the gap junction blocker carbenoxolone at 100 μM. **(I)** AEI charge in
278 the presence of carbenoxolone at 100 μM. Each dot shows one cell; lines show mean ± SEM; n = 9 cells from
279 N = 4 mice. **(J)** Schematic showing the potential involvement in the AEI response of neighbouring GABAergic
280 neurons activated by depolarising GABA released from the patched cell. **(K)** Example trace of an AEI response
281 in the presence of the NKCC1 channel blocker bumetanide at 20 μM. **(L)** AEI charge in the presence of
282 bumetanide at 20 μM. All conventions as in F; n = 5 cells from N = 3 mice.

283

284 Glomerular neurons are electrically coupled via gap junctions (Schoppa and Westbrook, 2002;
285 Kosaka et al., 2005; Banerjee et al., 2015). To exclude the possibility that the electrical activation of
286 neighbouring, GABA-releasing neurons is mediating the AEI response (**Figure 4G**), we showed that
287 AEI was still present after gap junctions were pharmacologically blocked with 100 μM carbenoxolone
288 (**Figure 4H, I**; AEI charge after blockers: 16.27 ± 3.83 pC; n = 9 cells from N = 4 mice).

289 Finally, another source of activation of neighbouring GABA-releasing neurons could be GABA itself:
290 GABA can have depolarising effects on glomerular layer neurons (Parsa et al., 2015). To show that
291 the GABA released by the recorded neuron is not activating neighbouring GABA-releasing cells
292 (**Figure 4J**), we recorded strong AEI responses when depolarising GABA responses were prevented in
293 the presence of the Na-K-Cl cotransporter 1 (NKCC1) blocker bumetanide used at 20 μM (**Figure 4K,**
294 **L**; AEI charge after blockers: 32.86 ± 13.66; n = 5 cells from N = 3 mice). Altogether, these data
295 robustly demonstrate that the AEI response in anaxonic DA neurons indicates true self-inhibition.

296

297 **Axon-bearing DA neurons do not self-inhibit**

298 We next wanted to assess whether axon-bearing DA neurons can self-inhibit. In light of our
299 anatomical data showing the presence of release sites exclusively on the distal axon, we predicted
300 that these cells do not exert synaptic inputs onto themselves. Using the same DAT-tdT mouse line to
301 label DA neurons, we identified tdT+ axon-bearing DA neurons by their characteristic 'biphasic'
302 action potential waveform (**Figure 5A**, Galliano et al., 2018; Galliano et al., 2021; Tufo et al., 2025).
303 Consistent with axon-bearing neurons having larger soma sizes than their anaxonic counterparts
304 (Kosaka and Kosaka, 2008; Galliano et al., 2018; **Figure 3D, Supplementary Figure 2A**), we found that
305 axon-bearing DA neurons exhibited significantly lower input resistance and a non-significant trend
306 towards higher membrane capacitance compared to anaxonic DA neurons (**Supplementary Figure**
307 **4A, B**; input resistance: 324.0 ± 31.93 MΩ for axon-bearing DA neurons, n=11 cells from N=8 mice;
308 683.8 ± 47.11 MΩ for anaxonic DA cells, n=45 cells from N=32 mice, p<0.0001, Mann-Whitney test.
309 Membrane capacitance: 46.08 ± 4.79 pF for axon-bearing DA neurons, n=11 cells from N=8 mice;
310 41.57 ± 1.35 pF for anaxonic DA cells, n=45 cells from N=32 mice, p=0.50, Mann Whitney test).

311 As predicted, GABA-mediated AEI currents were lacking in almost all axon-bearing DA neurons
312 (**Figure 5B, C;** 8/9 cells from N = 5 mice, = 89 %; mean ± SEM AEI charge for axon-bearing neurons:
313 3.8 ± 2.8 pC; n = 9 cells from N = 5 mice; anaxonic cells: 44.11 ± 6.02 pC; n = 31 cells from N = 18
314 mice; Mann-Whitney test, $p < 0.0001$) despite these neurons having functional GABA-A receptors as
315 shown by the presence of prominent gabazine-sensitive spontaneous IPSCs (**Figure 5D;** n = 9 axon-
316 bearing neurons from N = 5 mice; n = 31 anaxonic cells from N = 18 mice). Even when we attempted
317 to maximise AEI amplitude via a paired-pulse protocol (Bouhours et al., 2011) or prolonged
318 depolarisation, we still saw no evidence of self-inhibition in this cell subtype (**Figure 5E, F,**
319 **Supplementary Figure 4C, D;** AEI charge for single response: 5.4 ± 2.61 pC; n = 8 cells from N = 7
320 mice; AEI charge for paired response: 1.51 ± 2.91 pC; n = 8 cells from N = 7 mice; Wilcoxon matched-
321 pairs signed rank test, p = 0.06. AEI charge for 10 ms response: 0.26 ± 0.21 pC, n = 7 cells from N = 6
322 mice; AEI charge for 100 ms response: 7.75 ± 7.51 pC; n = 7 cells from N = 6 mice; Wilcoxon
323 matched-pairs signed rank test, p = 0.30). Axon-bearing DA neurons did produce a tail current in
324 response to the AEI protocol; however, this was insensitive to gabazine and was instead abolished by
325 adding the voltage-gated calcium channel blocker cadmium at 200 μM (**Figure 5G and**
326 **Supplementary Figure 4E;** average cadmium sensitive current: 15.33 ± 6.95 pC, n=3 cells from N=3
327 mice).
328
329 In conclusion, these findings provide both structural and functional evidence showing that anaxonic
330 DA neurons in the OB can signal locally, even to the point of self-inhibition. In contrast, axon-bearing
331 DA neurons can – unlike all other major cell types in this brain region – only release
332 neurotransmitters distally from their axon.

Figure 5

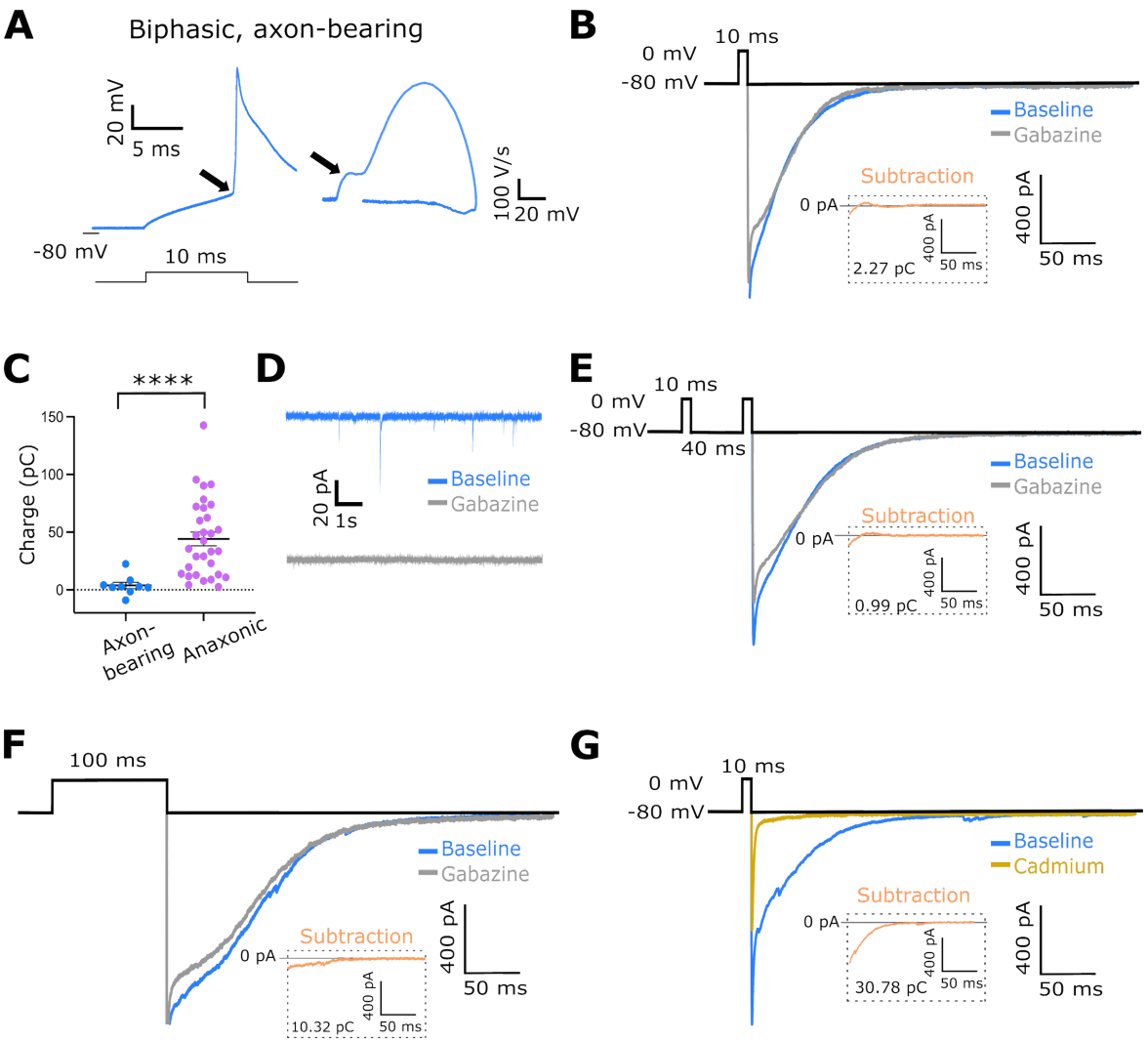

Figure 5. **Axon-bearing DA neurons do not self-inhibit. (A)** Example trace of an action potential fired by a putative axon-bearing DA neuron (left) and its biphasic phase-plane plot profile (right). Arrows point to spike onset kink (left) and initial segment bump (right). Note the prolonged repolarisation due to Cs-based internal solution. **(B)** Example traces showing tail current responses in an axon-bearing DA neuron before (blue) and after (grey) the application of gabazine. The subtraction is shown in the orange inset trace. **(C)** AEI charge in axon-bearing and anaxonic DA neurons. Each dot shows one cell; lines show mean ± SEM; n = 9 axon-bearing cells, n = 31 anaxonic cells from N = 18 mice; Mann-Whitney test; ****, $p < 0.0001$. **(D)** Example traces showing spontaneous IPSCs in an axon-bearing DA neuron before (blue) and after (grey) the application of gabazine. **(E), (F)** Example traces showing tail current responses in axon-bearing DA neurons before (blue) and after (grey) the application of gabazine using a paired-pulse protocol **(E)** and prolonged depolarisation **(F)**. Subtractions are shown in the orange inset traces. **(G)** Example traces showing that the tail current recorded in axon-bearing DA neurons (blue) is blocked by cadmium (ocre). The subtraction is shown in the orange inset trace.

Discussion

Our results show that different polarity-defined dopaminergic (DA) subtypes in the olfactory bulb use distinct anatomical compartments for neurotransmitter release. While anaxonic DA neurons release from the dendrites, axon-bearing DA cells release nearly exclusively from the axon. These anatomical findings correlate strongly with different function: anaxonic DA neurons can self-inhibit, but this ability is absent in almost all of the axon-bearing DA population.

The link between neuronal polarity and neurotransmitter release

Our anatomical data indicate that anaxonic DA neurons have release sites on their dendrites, while the presynaptic sites of almost all the axon-bearing DA cells are located exclusively on their intermittently myelinated axons. These findings are entirely consistent with previous descriptions of release site localisation in similar OB cell types. Early ultrastructural work showed the absence of release sites in the dendrites of axon-bearing neurons in the glomerular layer, defined morphologically as 'short-axon cells' (Pinching and Powell, 1971). It was also shown that axon-bearing DA neurons located in the external plexiform layer do not have dendritic release sites (Liberia et al., 2012). In contrast, further ultrastructural work revealed the presence of release sites in the dendrites of small DA periglomerular neurons, presumably anaxonic (Kiyokage et al., 2017). Our results agree with all of these findings while specifically assigning different neurotransmitter release strategies to axon-bearing and anaxonic DA neurons.

We have shown that anaxonic DA neurons use their only available anatomical compartment, the dendrites, to release neurotransmitters. This paradigm of anaxonic structural and functional polarity is unconventional but is found in other neuron types, including amacrine cells in the retina and OB granule cells (Wu et al., 2011; Marshak, 2016; Nunes and Kuner, 2018). In fact, dendritic release is not an uncommon phenomenon in the brain and is observed even in many axon-bearing neurons. Dopaminergic neurons in the midbrain, for example, are one of the most studied examples of dendritic release (Cheramy et al., 1981; Hikima et al., 2021). In the olfactory bulb, most neurons with axodendritic polarity can release from both the axon and the dendrites, including mitral cells and external tufted cells (Isaacson and Strowbridge, 1998; Schoppa and Urban, 2003; Hayar et al., 2004)**.** In this context, axon-bearing OB DA neurons are unique: they do not have dendritic release despite their dopaminergic nature, and despite their identity as OB neurons with classic axodendritic polarity.

OB DA neurons co-release both GABA and dopamine (Wachowiak and Cohen, 1999; Berkowicz and Trombley, 2000; Borisovska et al., 2013, Liu et al., 2013; Vaaga et al., 2017; Banerjee et al., 2015), so do their distinct release strategies apply to both transmitters? Our anatomical approach reliably detects GABA presynaptic sites, with a high percentage of co-localisation between synaptophysin-mRuby and vGAT (**Figure 1E**). However, not all synaptophysin-mRuby puncta are vGAT-positive. This could reflect technical limitations in release site detection (Risher et al., 2015; Heise et al., 2016), but also indicates that vGAT-negative spots may represent specific dopamine release sites (Borisovska et al., 2013; Liu et al., 2013; Vaaga et al., 2017). Indeed, in other brain regions synaptophysin-mRuby puncta have been used to reveal sites of dopamine release (Li et al., 2005). In OB DA neurons GABA and dopamine release are associated with different functions (Lyons-Warren et al., 2023) and the two transmitters are known not to be released from the same vesicles (Borisovska et al., 2013). However, this does not necessarily imply that they are released from different active zones. Addressing this question in the current study was unfortunately not possible due to notorious

394 difficulties in staining the dopamine vesicular transporter 2 (VMAT2) due to the lack of effective
395 commercially available antibodies (Zhang et al., 2015; Jain et al., 2023). Whether anaxonic and axon-
396 bearing DA neurons release dopamine and GABA from the same sites remains an important question
397 for future studies.

398 In light of our findings, many fascinating questions about anaxonic DA neurons remain to be
399 explored. How is dendritic release developed and maintained throughout the life of the neuron?
400 Specific mechanisms have been identified that drive the establishment and maintenance of neuronal
401 polarity in neurons with a classic axodendritic configuration (for reviews see Rasband, 2010; Lalli,
402 2014; Bentley and Banker, 2016). Do some of these molecular events, like cytoskeleton
403 reorganisation and/or trafficking processes, differ in the dendrites of anaxonic neurons versus the
404 'standard' dendrites of axon-bearing neurons? Future work will answer these and further questions
405 on the developmental and functional intricacies of unconventional neurons in the brain.

406

407 **Does dendritic release equal self-inhibition?**

408

409 Self-inhibition in the olfactory bulb was initially discovered in a subset of periglomerular cells (Smith
410 and Jahr, 2002) and later described specifically in dopaminergic neurons (Maher and Westbrook,
411 2008). Here, we find that self-inhibition is not a universal OB DA neuron feature, but instead is an
412 almost exclusive property of anaxonic DA cells. By ruling out potential external sources of GABA in
413 the glomerular circuit, we have also provided the clearest evidence to date for true self-inhibition in
414 OB periglomerular cells.

415 The link between dendritic release of neurotransmitters and self-inhibition exists in other brain
416 regions as well. Neurons in the substantia nigra release dopamine that binds to auto-receptors and
417 subsequently inhibits the neuron (Pucak and Grace, 1994; Falkenburger et al., 2001). Other examples
418 include noradrenergic neurons in the locus coeruleus and serotonergic cells in the nucleus raphe
419 dorsalis (Aghajanian et al., 1977; Liu et al., 2005). However, while these neurons have a classic
420 axodendritic polarity and are able to release from their axons as well, anaxonic DA cells constitute a
421 distinct model as dendrites are the solely available compartment for such function.

422 Finally, does dopamine released from an anaxonic OB DA neuron also modulate that same neuron?
423 Our own data demonstrate that the auto-evoked inhibition current is purely GABAergic: it is
424 suppressed after the application of gabazine, but unaffected after blocking dopamine receptors
425 (**Figure 4C, E, F**). In addition, our transcriptomic data clearly show that OB DA neurons do not
426 express dopamine receptors at all (**Figure 4A**). It is therefore unlikely there is a dopaminergic
427 component to the self-inhibition response. Previous reports of dopamine-driven responses in OB DA
428 neurons (Liu, 2020) may instead have occurred via well-described gap junction connectivity between
429 DA cells and dopamine-responsive ETCs (Liu et al.2013; Banerjee et al., 2015).

430

431 **Implications for information processing**

432 Anaxonic DA neurons release neurotransmitters from their dendrites, which are confined to local
433 areas of the glomerular layer. In contrast, axon-bearing DA cells release from their axons, which
434 spread for long distances across the glomerular layer (Kosaka and Kosaka, 2008; Galliano et al.,
435 2018). Our findings lead to the prediction of a clear division of circuit function for very closely related

436 cell subtypes: anaxonic DA neurons take part in local, intraglomerular inhibition, while axon-bearing
437 DA cells participate in distal, interglomerular inhibition.

438 Functionally, intraglomerular inhibition acts as 'high pass filter' for weak odour signals detected in a
439 glomerulus, enhancing the contrast between different olfactory stimuli (Shao et al., 2012; Gire and
440 Schoppa, 2009; Zak and Schoppa, 2021). Anaxonic DA neurons are therefore expected to contribute
441 to intraglomerular inhibition via different pathways which have been generally described for
442 periglomerular cells. This includes the exclusively intraglomerular presynaptic inhibition of olfactory
443 sensory neurons (Hsia et al., 1999; Ennis et al., 2001; McGann et al., 2005; Korshunov et al., 2017;
444 McGann 2013; Vaaga et al., 2017), as well as the dendrodendritic inhibition of multiple neighbouring
445 glomerular cell types, including interneurons and projection neurons (Murphy et al., 2005; Gire and
446 Schoppa, 2009). We observed heterogeneity in the puncta density along the dendrites of anaxonic
447 DA neurons which, potential technical considerations notwithstanding, suggests that dendritic
448 neurotransmitter release is not uniform across these cells. This variability may reflect differences in
449 spatial positioning within the glomeruli, potentially aligning synaptic output with local circuit
450 demands and individual postsynaptic partner types.

451 Self-inhibition would be expected to decrease the capacity of anaxonic DA neurons to release GABA
452 over time, therefore reducing inhibitory influence within glomerular circuits. Self-inhibition could
453 therefore control the timing of intraglomerular inhibition, allowing subsequent stimuli to activate
454 glomerular networks. Self-inhibition could also aid the high-pass filter function of glomerular
455 networks (Gire and Schoppa, 2009). If it occurs exclusively in the context of strong DA neuron
456 activation, it could decrease intraglomerular inhibition to promote glomerular output when input
457 strength goes past a certain threshold. There is also the possibility that self-inhibition is more of a
458 bug than a feature. Perhaps if anaxonic DA neurons have to release GABA from their dendrites in
459 order to perform their intraglomerular circuit functions, the chances are high that their nearby
460 postsynaptic receptors cannot escape some of that GABAergic influence. Further work is needed to
461 investigate how these mechanisms influence overall intraglomerular inhibition and glomerular
462 output.

463 Glomeruli in the olfactory bulb create a spatial map of odour identity, where different odours
464 specifically activate different combinations of glomeruli (Soucy et al., 2009; Murthy, 2011).
465 Interglomerular inhibition acting between different glomeruli selectively enhances the signal
466 contrast in between individual stimuli, boosting odour identification and/or discrimination (Uchida
467 et al., 2000; Urban, 2002). This circuit function must be exclusively undertaken by axon-bearing DA
468 neurons, due to their unique capacity for long-range axonal release of neurotransmitters (this paper;
469 Kosaka & Kosaka, 2008; Liu et al., 2013; Whitesell et al., 2013; Banerjee et al., 2015).

470 Several key traits are shared across the entire population of OB DA neurons, including their
471 dopaminergic and GABAergic identities and their glomerular location in the olfactory circuitry.
472 Despite these similarities, we have found fundamental differences between OB DA subtypes in terms
473 of their anatomy, neurotransmitter release compartments and the presence/absence of self-
474 inhibition. These are strong foundations to suggest entirely different sensory processing functions in
475 even very closely related interneuron sub-populations.

476

477

478

Materials and Methods

Animals

We used mice of either sex and housed them under a 12h light-dark cycle in an environmentally controlled room with access to water and food *ad libitum*. Wild-type C57/Bl6 mice (Charles River) were used either as experimental animals, or to back-cross each generation of transgenic animals. The founders of our transgenic mouse lines – vGAT-cre (Slc32a1$^{tm2(cre)Lowl}$/J, Jax stock 016962), DAT-cre (B6.SJL-Slc6a3$^{tm1.1(cre)Bkmn}$/J, Jax stock 006660) and flex-tdT(B6.Cg–Gt(ROSA)26Sor$^{tm9(CAG-tdTomato)Hze}$/J , Jax stock 007909) were purchased from The Jackson Laboratory. Immunohistochemistry experiments with vGAT-cre mice were performed at postnatal day (P)28. Patch-clamp electrophysiology experiments with DAT-tdT mice were performed between P21-P35. All experiments were performed in accordance with the United Kingdom Animals (Scientific Procedures) Act 1986, under the auspices of Home Office personal and project licenses held by the authors.

Viral injections

To sparsely label neuronal morphology together with presynaptic release sites, vGAT-cre mice were injected *in utero* via intraventricular injection with AAV-DJ-hSyn-FLEx-mGFP-T2A-Synaptophysin-mRuby (3 x 10^{12} GC/ml, AAV DJ GVVC-AAV-100, Stanford Vector Core Facility) (Beier et al., 2015; Kathe et al., 2022) at embryonic day (E)14. Time-mated pregnant mice were anaesthetised with isoflurane, used at 4% for general anaesthesia induction and at 2% for anaesthesia maintenance. Injections (≈1µl) were performed with a glass-pulled pipette (1B150-F4, World Precision Instruments) through the uterine wall into one of the lateral ventricles of the embryos. The uterine horns were then returned into the abdominal cavity, the wall and the skin were sutured, and the embryos were allowed to continue their development *in utero* and born naturally until experimental use. Post-surgery, mice recovered in a 32°C chamber and were housed individually.

Immunohistochemistry

P28 and P33 mice were anaesthetised with an overdose of pentobarbital and then perfused with 20-25 ml of PBS with heparin (A16198, Thermo Fisher Scientific) (20 units/mL), followed by 20-25 ml of 4% paraformaldehyde (PFA; P001, TAAB Laboratories) in 3% sucrose, 60 mM PIPES, 25 mM HEPES, 5 mM EGTA, and 1 mM $MgCl_2$ (all purchased from Sigma-Aldrich). The olfactory bulbs were dissected and post-fixed in 4% PFA overnight (4°C), then embedded in 5% agarose and sliced at 50 µm using a vibratome (VT1000S, Leica). Free-floating slices were washed with PBS 1x and permeabilised and blocked in PBS with 5% normal goat serum (NGS, G9023, Sigma-Aldrich) and 0.25% Triton (Triton X100, Sigma-Aldrich) for 2 hr at room temperature (RT). Slices were then incubated in primary antibody solution (antibodies diluted in PBS with 5% and 0.25% Triton) for 2-5 days at 4°C. Primary antibodies, working dilutions and sources are indicated in Table 1. Slices were then washed three times for 10 minutes with PBS, before being incubated in secondary antibody solution (species-appropriate Life Technologies Alexa Fluor-conjugated; all at a 1:1000 dilution in PBS with 5% NGS and 0.25% Triton) for 2h at RT. After washing 3 times for 10 minutes with PBS, slices were mounted on glass slides (J2800AMNZ, Epredia) with FluorSave (345789, Merck).

All immunostainings involving multiple targets were performed by incubating the primary antibodies simultaneously, except for the combination of mouse anti-TH and rat anti-MBP, where a sequential incubation was necessary to avoid cross-reactivity (first TH, then MBP).

522

523 *Table 1. Primary antibodies.*

Target	Host	Dilution	Supplier	Reference	Identifier
TH	Mouse	1:500 1:5000 1:10000 1:50000	Merck	MAB318	RRID:AB_2201528
GFP	Chicken	1:1000	Abcam	ab13970	RRID:AB_300798
TRIM46	Guinea pig	1:500	Synaptic Systems	377005	RRID:AB_2721101
vGAT	Rabbit	1:1000	Synaptic Systems	131002	RRID:AB_887871
mCherry	Rat	1:500	Thermo Fisher	M11217	RRID:AB_2536611
MBP	Rabbit	1:1000	Thermo Fisher	PA5-78397	RRID:AB_2736178
MBP	Rat	1:500	Millipore	MAB386	RRID:AB_94975
Synaptophysin	Guinea pig	1:500	Synaptic Systems	101004	RRID:AB_1210382

524

525

526 **Image acquisition, analysis, and illustration**

527 *Acquisition*

528 All images were acquired using a laser scanning confocal microscope (Zeiss LSM 710, equipped with
529 Zen 2010 B-SP1 software) using appropriate excitation and emission filters, a pinhole of 1 AU and
530 40x or 63x oil immersion objectives. Laser power and gain were set to prevent fluorescence
531 saturation and allow acquisition with an optimal signal-to-noise ratio, and z-stacks were acquired at
532 software-defined optimal thickness and step sizes. For puncta detection and dendritic
533 reconstruction, stacks were acquired with 1x zoom (0.033 μm/pixel), 2048 x 2048 pixels, and in z-
534 stacks with 0.37 μm steps. The dopaminergic identity of the cells was assessed qualitatively by taking
535 a single plane snapshot of the TH and GFP channels that included the soma. Analysed cells were
536 located exclusively in the OB's glomerular layer, including the border with the external plexiform
537 layer. Axon-bearing neurons displayed at least one clear elongated TRIM46-positive region (of
538 approximately 10 to 25 μm in length) that belonged to a GFP+ process. For co-localisation analyses,
539 stacks were acquired with 2x zoom (0.033 μm/pixel), 2048 x 2048 pixels, and in z-stacks with 0.37μm
540 steps. Due to the low penetration of the vGAT antibody, and following similar studies (Heise et al.,

541 2016), these stacks were thinner (1.1-1.2 μm total depth) to capture most of the signal and perform
542 reliable co-localisation assessment.

543

544 *Analysis*

545 Puncta detection and dendritic tracing in 3D stacks were performed using Imaris (version 9.1.2).
546 Individual stacks were carefully examined in three dimensions by rotating the images and adjusting
547 the zoom to ensure accurate identification of neuronal processes belonging to specific neurons. Cells
548 for which this could not be confirmed were excluded from the analysis. Synaptophysin-mRuby
549 belonging to specific GFP processes were detected based on their signal overlap with GFP. To
550 automate puncta detection, synaptophysin-mRuby and gephyrin puncta were detected by
551 estimating a punctum size of 0.5 μm and then using the 'Quality' filter. Detection threshold was kept
552 within an unbiased consistent range (1000 to 2700) that allowed adaptation to variability between
553 staining experiments and mice. Dendritic traces were performed using the 'Filaments' function, and
554 the total length and maximum length of dendrites were calculated accordingly. Puncta density was
555 estimated by dividing the total number of puncta by the total length of dendrites.

556 For co-localisation analysis, the 3-dimensional centroid coordinates for the synaptophysin-mRuby
557 puncta detected in Imaris were exported and analysed using a custom-written script in Matlab. This
558 determined, at the y- and z-axis centroid co-ordinates of each mRuby punctum, the vGAT
559 fluorescence intensity averaged over a 1 μm window centred on the local maximum of the mRuby
560 distribution's x-position. If this mRuby-centred vGAT fluorescence intensity was greater than 1
561 standard deviation higher than local background vGAT fluorescence (taken from a 1 μm window
562 immediately outside the x-axis border of the mRuby punctum), the punctum was considered to be
563 'co-localised.' The overall percentage of co-localised puncta was then determined for each cell.

564 For soma size measurements, 3D stacks were first transformed into maximum intensity projections.
565 We used the polygon drawing tool on Fiji (Schindelin et al., 2012) to draw the soma and obtained the
566 area measurements using the 'measure' function.

567

568 *Illustration*

569 All images in the manuscript displaying examples of immunostaining were taken as high-resolution
570 snapshots on ImarisViewer (version 10.2.0). Image stitching in Figure 3 was performed using
571 maximum intensity projections of individual stacks that were assembled using the ImageJ plugin
572 MosaicJ (Thevenaz and Unser, 2007). Orthogonal views in Figure 1F were created in Fiji (Schindelin
573 et al., 2012). Schematics, drawings, and figures layouts were designed using Inkscape (version 1.3.2).

574

575 **Acute slice preparation**

576 DAT-tdT mice at P21-35 were decapitated under isoflurane anaesthesia, and the olfactory bulb was
577 removed and transferred into ice-cold slicing medium containing (in mM): 240 sucrose, 5 KCl, 1.25
578 Na_2HPO_4, 2 $MgSO_4$, 1 $CaCl_2$, 26 $NaHCO_3$ and 10 D-Glucose (all reagents from Sigma-Aldrich), bubbled
579 with 95% O_2 and 5% CO_2. Horizontal slices (300 μm) of the olfactory bulb were cut using a vibratome
580 (VT1000S, Leica and 7000 smz-2, Campden Instruments) and maintained in artificial cerebrospinal
581 fluid (ACSF) containing (in mM): 124 NaCl, 2.5 KCl, 1.25 Na_2HPO_4, 2 $MgSO_4$, 2 $CaCl_2$, 26 $NaHCO_3$ and

582 15 D-Glucose, bubbled with 95% O_2 and 5% CO_2. Slices were kept for 30 minutes in a water bath at
583 34 °C and then left to recover for 30 minutes at room temperature (RT).

584

585 **Acute slice electrophysiology**

586 Individual slices were placed in a chamber mounted on a FN1 Fixed Stage Nikon microscope and held
587 in place with a stainless-steel slice anchor. Slices were continuously superfused with ACSF heated to
588 physiologically relevant temperature (34 ± 1°C) using an in-line solution heater (TC-344B, Warner
589 Instruments). The ACSF contained, at all times, the NMDA receptor blocker DL-2-Amino-5-
590 phosphonopentanoic acid at 50 µM (APV; A5282, Sigma-Aldrich), the AMPA receptor blocker 2,3-
591 dioxo-6-nitro-7-sulfamoyl-benzo[f]quinoxaline at 10 µM] (NBQX; N183, Sigma-Aldrich). The sodium
592 channel blocking tetrodoxin citrate (TTX; T-550, Alomone and 1069, Tocris) was used at 10 µM for all
593 experiments excluding action potential recordings. Block of GABA-A receptors was achieved by the
594 application of SR-95531 gabazine (1262, Tocris) for 5 minutes in the bath at 10 µM and confirmed by
595 the absence of IPSCs. D1-like and D2-like receptors were blocked by applying SKF 83566
596 hydrobromide for 5 minutes in the bath at 10 µM (1586, Tocris) and sulpiride at 10 µM (S8010,
597 Sigma-Aldrich), respectively. Calcium channels were blocked by applying cadmium chloride (202908,
598 Sigma) at 200 µM for 5 minutes in the bath. The gap junction blocker carbenoxolone disodium at 100
599 µM (3096, Tocris) and the NKCC1 blocker bumetanide at 20 µM (3108, Tocris) were applied in the
600 bath from the beginning and kept in the ACSF for at least 20-40 minutes. We adopted this strategy
601 due to two key considerations: (1) carbenoxolone induced instability in the membrane properties of
602 the neurons during the initial minutes of application, and (2) sufficient time was required for
603 chloride transporters to reach a steady intracellular chloride concentration ([Cl^-]) in response to
604 bumetanide.

605 Recording pipettes were pulled from borosilicate glass (1B150F-4, World Precision Instruments) with
606 a vertical puller (PC-10, Narishige). Some were tip fire-polished with a microforge (MF-830,
607 Narishige). All auto-evoked inhibition (AEI) recordings were performed using caesium chloride
608 intracellular solution (in mM: 125 CsCl, 10 HEPES, 0.1 EGTA, 4 MgATP, 0.3 Na_3GTP, 10
609 phosphocreatine, 10 GABA (280-290 mOsm and pHed to ~7.3 with CsOH), and pipette resistances of
610 2-4 MΩ.

611

612 *Auto-evoked inhibition recordings*

613 DAT-tdT neurons were visualised with a 40x water immersion objective and tdT fluorescence was
614 revealed by LED excitation (CoolLED pE-100) with appropriate excitation and emission filters. All
615 recorded cells were located in the OB's glomerular layer, including the border with the external
616 plexiform layer. To ensure specificity in targeting only dopaminergic neurons, we avoided small,
617 dimly fluorescent neurons which are likely to be of the calretinin-expressing glomerular subtype and
618 excluded from our data any recordings showing evidence of those calretinin-positive cells'
619 characteristically unstable and weak spiking (Benito et al., 2018; Byrne et al., 2022). Recordings were
620 performed using a HEKA EPC 10/2 amplifier coupled to PatchMaster acquisition software (HEKA
621 Elektronik). Signals were digitised and sampled at 20 kHz (50 µs interval sample) unless otherwise
622 stated, and Bessel filtered at 10 kHz (filter 1) and 2.9 kHz (filter 2; active filters used in voltage clamp
623 only).

624 Axon-bearing and anaxonic DA neurons were identified based on their action potential waveform.
625 For that, cells were held at -60 mV in current clamp with 100% bridge balance. 10 ms somatic
626 current injections of Δ+5 pA steps were applied until threshold was reached and an action potential
627 occurred. 10 ms duration current injections were sampled at high temporal resolution 200 kHz (5 μs
628 sample interval) and the recordings were smoothed prior to differentiation using a 20 point (100 μs)
629 sliding filter. The first derivative of the smoothed trace was used for dV/dt and phase plane plot
630 analyses. Neurons were then visually determined as axon-bearing or anaxonic based on their
631 biphasic or monophasic phase plane plot profiles, respectively (Galliano et al., 2018).

632 Spontaneous IPSCs were recorded as inward events at –80 mV for 1 minute while 1 μM TTX was
633 added to the ACSF. Sodium channel block was confirmed by running an IV protocol and observing
634 the block of the large, inward sodium current.

635 AEI recordings were sampled at 50 kHz (20 μs sample interval), with slow capacitance compensated.
636 After membrane rupture, a test series was performed in voltage-clamp mode. The average current
637 response to a double test pulse (5 ms steps, -10 and +10 mV) from the holding voltage of -60 mV was
638 used to estimate series resistance (R_S; peak current), input resistance (R_I; steady-state holding
639 current at new voltage) and membrane capacitance (C_M; area under the exponentially decaying
640 current from peak to steady-state current). Series resistance (R_S) was assessed continuously and
641 recordings were excluded if they exceeded 30 MΩ at any point or changed more 30% during any
642 recording.

643 AEI protocols were performed in voltage-clamp from a holding potential of –80 mV, unless otherwise
644 stated. Neurons were depolarised to 0 mV for 10 or 100 ms, before returning to –80 mV. Paired
645 recordings were two 10 ms duration voltage steps with 50 ms inter-stimulus interval. All protocols
646 were repeated 3 times, with 30 seconds in between each sweep, and an average response
647 calculated. Due to the presence of passive currents, sweeps were analysed from 10 ms after the end
648 of the voltage step for 500 ms. Gabazine and cadmium-sensitive AEI currents were measured as the
649 difference between the pre- and the post-treatment averaged traces. The final charge was
650 calculated as the area under the curve of the subtracted response. For AEI decay kinetics analysis,
651 the time constant k was measured from a single exponential function fitted to the average response
652 over the same timeframe used for charge calculation.

653 We confirmed no change in the AEI response over time by repeating the 10 ms voltage step protocol
654 3 times, with 5 minutes in between each protocol. No significant change in the charge of the AEI
655 response was found during the experiment (**Supplementary Figure 5A**; mean ± SEM: timepoint 1, 25
656 ± 7.99 pC; timepoint 2, 27.29 ± 9.57 pC; timepoint 3, 29.29 ± 11.22 pC; n = 5, N = 4 mice; one-way
657 repeated measures ANOVA, p = 0.44). We also ruled out the effect of somatic depolarisation on the
658 AEI response by holding the DA neurons either at -50 mV or -80 mV for approximately 30 seconds
659 before the start of the recordings. Neurons were then depolarised to 0 mV for 10 ms and then
660 brought to -80 mV. The AEI response was not different between holding at -50 mV or -80 mV
661 (**Supplementary Figure 5B**; mean ± SEM: -50 mV response, 25.45 ± 4.53 pC; -80 mV response, 25.3 ±
662 7.3 pC; n = 5, N = 3 mice, paired t-test, p = 0.96). These results suggest that our experimental design
663 produces a reliable and stable response to study auto-evoked inhibition in this neuronal population.

664

665 **Data analysis**

666 For RNAseq data plotting, we made use of a whole olfactory bulb single cell RNAseq dataset (Brann
667 et al., 2020), that integrates data from juvenile and adult mouse samples, contains labels for

identified clusters for the different cell types, and for visualising the expression of genes of interest in identified cell types from the olfactory bulb. Details about data processing, cluster inference and annotation can be found in the original publication. Briefly, graph-based clustering was performed using the Louvain algorithm and cluster stability evaluated using Clustree. The clusters were annotated using known gene expression markers. Here, cluster 11 corresponds to the dopaminergic neurons and contained 1453 cells. These were identified by their expression of known olfactory bulb dopaminergic neuron markers, including *Th*, *Trh*, *Pax6*, amongst others. Violin plots depicting the expression of *Th*, *Syp* (Synaptophysin), *Slc32a1* (vGAT), and the dopamine receptors *Ddr1-5*, in the cell cluster corresponding to the dopaminergic neurons, were generated with the R package Seurat. The dataset is available for download in the accompanying supplementary data, alongside the code used for generating the figures.

Data analysis, statistical analysis and plotting were carried out using GraphPad (San Diego, CA), R and custom-written Matlab (Mathworks) scripts. Data are reported as mean ± SEM unless otherwise stated. 'N' represents the number of mice and 'n' is the number of cells. Details of individual statistical tests can be found in the results section and in figure legends. Data sets were tested for normality using the D'Agostino and Pearson tests where the datasets were sufficiently large, and Shapiro-Wilk test if not. Statistical tests were determined considering the distribution of the data (normal or non-normal) and sample variance (equal or unequal). All tests were two-tailed, with $\alpha = 0.05$. Our experiments addressed questions of cellular morphology and function, and datasets comprised few neurons per animal, so comparisons were performed with cell as the unit of analysis. However, for all significant results, where false positive inflation due to pseudoreplicate data is of highest concern, we additionally performed nested analyses that took intra-animal data dependence into account (Aarts et al., 2014). In all cases, these nested tests also returned significant differences between anaxonic and axon-bearing cell types.

Data availability statement

The full raw dataset supporting this article will be openly available upon manuscript acceptance in a peer-reviewed journal at the King's College London research repository (reserved DOI: 10.18742/27731157).

Author contributions

DJB and MSG designed experiments; AD-R, DJB, YL, MC, CA and MCF performed experiments; AD-R, DJB, YL, ML and MSG analysed data, AD-R and MSG wrote the paper.

Acknowledgements

This work was supported by a Wellcome Trust Early-Career Award to AD-R and MSG (227621/Z/23/Z); BBSRC Research Grants (BB/V000195/1 and BB/N014650/1) and an H2020 ERC Consolidator Grant (FUNCOPLAN; 725729) to MSG; and an MRC Medical Research Council 4-year PhD studentship to DJB. We thank Elisa Galliano for valuable comments on the manuscript, the Andreae lab and the Centre for Developmental Neurobiology for image analysis support, Ikhlas Kechround and Nadine Leighton for immunostaining optimisation, the Burrone lab for advice on presynaptic labelling, Candida Tufo and Lorcan Browne for guidance and training in patch-clamp

electrophysiology, Wing Ka Lo for mouse work support and the current members of the Grubb lab for insightful discussions throughout the project.

References

Aarts, E., Verhage, M., Veenvliet, J. V., Dolan, C. V., & van der Sluis, S., 2014. A solution to dependency: Using multilevel analysis to accommodate nested data. Nature Neuroscience, 17(4), 491–496. https://doi.org/10.1038/nn.3648

Aghajanian, G.K., Cedarbaum, J.M., Wang, R.Y., 1977. Evidence for norepinephrine-mediated collateral inhibition of locus coeruleus neurons. Brain Research 136, 570–577. https://doi.org/10.1016/0006-8993(77)90083-X

Bäckman, C.M., Malik, N., Zhang, Y., Shan, L., Grinberg, A., Hoffer, B.J., Westphal, H., Tomac, A.C., 2006. Characterization of a mouse strain expressing Cre recombinase from the 3' untranslated region of the dopamine transporter locus. Genesis 44, 383–390. https://doi.org/10.1002/dvg.20228

Banerjee, A., Marbach, F., Anselmi, F., Koh, M.S., Davis, M.B., Garcia da Silva, P., Delevich, K., Oyibo, H.K., Gupta, P., Li, B., Albeanu, D.F., 2015. An Interglomerular Circuit Gates Glomerular Output and Implements Gain Control in the Mouse Olfactory Bulb. Neuron 87, 193–207. https://doi.org/10.1016/j.neuron.2015.06.019

Banker, G., 2018. The Development of Neuronal Polarity: A Retrospective View. Journal of Neuroscience 38, 1867–1873. https://doi.org/10.1523/JNEUROSCI.1372-16.2018

Batista-Brito, R., Close, J., Machold, R., Fishell, G., 2008. The Distinct Temporal Origins of Olfactory Bulb Interneuron Subtypes. Journal of Neuroscience 28, 3966–3975. https://doi.org/10.1523/JNEUROSCI.5625-07.2008

Beier, K.T., Steinberg, E.E., Deloach, K.E., Xie, S., Miyamachi, K., Schwarz, L., Gao, X.J., Kremer, E.J., Malenka, R.C., Luo, L., 2015. Circuit architecture of VTA dopamine neurons revealed by systematic input-output mapping. Cell, 162(3), 622–634. https://doi.org/10.1016/j.cell.2015.07.015.

Benito, N., Gaborieau, E., Diez, A. S., Kosar, S., Foucault, L., Raineteau, O., & Jan, D. D. S., 2018. A Pool of Postnatally Generated Interneurons Persists in an Immature Stage in the Olfactory Bulb. Journal of Neuroscience, 38(46), 9870–9882. https://doi.org/10.1523/JNEUROSCI.1216-18.2018

Bentley, M., Banker, G., 2016. The cellular mechanisms that maintain neuronal polarity. Nature Reviews Neuroscience 17, 611–622. https://doi.org/10.1038/nrn.2016.100

Berkowicz, D.A., Trombley, P.Q., 2000. Dopaminergic modulation at the olfactory nerve synapse. Brain Research 855, 90–99. https://doi.org/10.1016/S0006-8993(99)02342-2

Borisovska, M., Bensen, A.L., Chong, G., Westbrook, G.L., 2013. Distinct Modes of Dopamine and GABA Release in a Dual Transmitter Neuron. Journal of Neuroscience 33, 1790–1796. https://doi.org/10.1523/JNEUROSCI.4342-12.2013

Bouhours, Brice, Federico F. Trigo, and Alain Marty. 2011. 'Somatic Depolarization Enhances GABA Release in Cerebellar Interneurons via a Calcium/Protein Kinase C Pathway'. Journal of Neuroscience 31 (15): 5804–15. https://doi.org/10.1523/JNEUROSCI.5127-10.2011.

Brann, D.H., Tsukahara, T., Weinreb, C., Lipovsek, M., Van den Berge, K., Gong, B., Chance, R., Macaulay, I.C., Chou, H.-J., Fletcher, R.B., Das, D., Street, K., de Bezieux, H.R., Choi, Y.-G., Risso, D., Dudoit, S., Purdom, E., Mill, J., Hachem, R.A., Matsunami, H., Logan, D.W., Goldstein, B.J., Grubb, M.S., Ngai, J., Datta, S.R., 2020. Non-neuronal expression of SARS-CoV-2 entry genes in the olfactory system suggests mechanisms underlying COVID-19-associated anosmia. Science Advances 6, eabc5801. https://doi.org/10.1126/sciadv.abc5801.

Byrne, D. J., Lipovsek, M., Crespo, A., & Grubb, M. S., 2022. Brief sensory deprivation triggers plasticity of dopamine-synthesising enzyme expression in genetically labelled olfactory bulb dopaminergic neurons. European Journal of Neuroscience, 56(1), 3591–3612. https://doi.org/10.1111/ejn.15684

Castro, J.B., Urban, N.N., 2009. Subthreshold Glutamate Release from Mitral Cell Dendrites. Journal of Neuroscience 29, 7023–7030. https://doi.org/10.1523/JNEUROSCI.5606-08.2009

Chand, A.N., Galliano, E., Chesters, R.A., Grubb, M.S., 2015. A Distinct Subtype of Dopaminergic Interneuron Displays Inverted Structural Plasticity at the Axon Initial Segment. Journal of Neuroscience 35, 1573–1590. https://doi.org/10.1523/JNEUROSCI.3515-14.2015

Cheramy, A., Leviel, V., Glowinski, J., 1981. Dendritic release of dopamine in the substantia nigra. Nature 289, 537–542. https://doi.org/10.1038/289537a0

Coronas, V., Srivastava, L.K., Liang, J.-J., Jourdan, F., Moyse, E., 1997. Identification and localization of dopamine receptor subtypes in rat olfactory mucosa and bulb: a combined in situ hybridization and ligand binding radioautographic approach. Journal of Chemical Neuroanatomy 12, 243–257. https://doi.org/10.1016/S0891-0618(97)00215-9

Ennis, M., Zhou, F.-M., Ciombor, K.J., Aroniadou-Anderjaska, V., Hayar, A., Borrelli, E., Zimmer, L.A., Margolis, F., Shipley, M.T., 2001. Dopamine D2 Receptor–Mediated Presynaptic Inhibition of Olfactory Nerve Terminals. Journal of Neurophysiology 86, 2986–2997. https://doi.org/10.1152/jn.2001.86.6.2986

Falkenburger, B.H., Barstow, K.L., Mintz, I.M., 2001. Dendrodendritic Inhibition Through Reversal of Dopamine Transport. Science 293, 2465–2470. https://doi.org/10.1126/science.1060645

Galliano, E., Franzoni, E., Breton, M., Chand, A.N., Byrne, D.J., Murthy, V.N., Grubb, M.S., 2018. Embryonic and postnatal neurogenesis produce functionally distinct subclasses of dopaminergic neuron. eLife 7, e32373. https://doi.org/10.7554/eLife.32373

Garg, R., Kumar, V., Seiler, J. H., Wu, Y., McClain, M., Yi, K., & Yu, C. R., 2025. Dopaminergic short axon cells integrate sensory and top–down inputs to enhance discriminative learning in the mouse olfactory bulb. PLOS Biology, 23(9), e3003375. https://doi.org/10.1371/journal.pbio.3003375

Gire, D.H., Schoppa, N.E., 2009. Control of On/Off Glomerular Signaling by a Local GABAergic Microcircuit in the Olfactory Bulb. Journal of Neuroscience 29, 13454–13464. https://doi.org/10.1523/JNEUROSCI.2368-09.2009

Goaillard, J.-M., Moubarak, E., Tapia, M., Tell, F., 2020. Diversity of Axonal and Dendritic Contributions to Neuronal Output. Frontiers in Cellular Neuroscience 13.

Granseth, B., Odermatt, B., Royle, S.J., Lagnado, L., 2006. Clathrin-Mediated Endocytosis Is the Dominant Mechanism of Vesicle Retrieval at Hippocampal Synapses. Neuron 51, 773–786. https://doi.org/10.1016/j.neuron.2006.08.029

789 Hayar, A., Karnup, S., Ennis, M., Shipley, M.T., 2004. External Tufted Cells: A Major Excitatory
790 Element That Coordinates Glomerular Activity. Journal of Neuroscience 24, 6676–6685.
791 https://doi.org/10.1523/JNEUROSCI.1367-04.2004

792 Heise, C., Schroeder, J.C., Schoen, M., Halbedl, S., Reim, D., Woelfle, S., Kreutz, M.R., Schmeisser,
793 M.J., Boeckers, T.M., 2016. Selective Localization of Shanks to VGLUT1-Positive Excitatory Synapses
794 in the Mouse Hippocampus. Frontiers in Cellular Neuroscience 10.

795 Hikima, T., Lee, C.R., Witkovsky, P., Chesler, J., Ichtchenko, K., Rice, M.E., 2021. Activity-dependent
796 somatodendritic dopamine release in the substantia nigra autoinhibits the releasing neuron. Cell
797 Reports 35. https://doi.org/10.1016/j.celrep.2021.108951

798 Hökfelt, T., Halasz, N., Ljungdahl, Å., Johansson, O., Goldstein, M., & Park, D, 1975. Histochemical
799 support for a dopaminergic mechanism in the dendrites of certain periglomerular cells in the rat
800 olfactory bulb. Neuroscience Letters, 1(2), 85–90. https://doi.org/10.1016/0304-3940(75)90050-6

801 Hsia, A.Y., Vincent, J.-D., Lledo, P.-M., 1999. Dopamine Depresses Synaptic Inputs Into the Olfactory
802 Bulb. Journal of Neurophysiology 82, 1082–1085. https://doi.org/10.1152/jn.1999.82.2.1082

803 Imamura, F., Ito, A., LaFever, B.J., 2020. Subpopulations of Projection Neurons in the Olfactory Bulb.
804 Frontiers in Neural Circuits 14. https://doi.org/10.3389/fncir.2020.561822

805 Isaacson, J.S., Strowbridge, B.W., 1998. Olfactory Reciprocal Synapses: Dendritic Signaling in the CNS.
806 Neuron 20, 749–761. https://doi.org/10.1016/S0896-6273(00)81013-2

807 Jain, S., Yee, A.G., Maas, J., Gierok, S., Xu, H., Stansil, J., Eriksen, J., Nelson, A.B., Silm, K., Ford, C.P.,
808 Edwards, R.H., 2023. Adaptor protein-3 produces synaptic vesicles that release phasic dopamine.
809 Proceedings of the National Academy of Sciences 120, e2309843120.
810 https://doi.org/10.1073/pnas.2309843120

811 Kathe, C., Skinnider, M.A., Hutson, T.H., Regazzi, N., Gautier, M., Demesmaeker, R., Komi, S., Ceto, S.,
812 James, N.D., Cho, N., Baud, L., Galan, K., Matson, K.J.E., Rowald, A., Kim, K., Wang, R., Minassian, K.,
813 Prior, J.O., Asboth, L., Barraud, Q., Lacour, S.P., Levine, A.J., Wagner, F., Bloch, J., Squair, J.W.,
814 Courtine, G., 2022. The neurons that restore walking after paralysis. Nature 611, 540–547.
815 https://doi.org/10.1038/s41586-022-05385-7

816 Kiyokage, E., Kobayashi, K., Toida, K., 2017. Spatial distribution of synapses on tyrosine hydroxylase–
817 expressing juxtaglomerular cells in the mouse olfactory glomerulus. Journal of Comparative
818 Neurology 525, 1059–1074. https://doi.org/10.1002/cne.24147

819 Korshunov, K.S., Blakemore, L.J., Trombley, P.Q., 2017. Dopamine: A Modulator of Circadian
820 Rhythms in the Central Nervous System. Frontiers in Cellular Neuroscience 11.
821 https://doi.org/10.3389/fncel.2017.00091

822 Kosaka, T., Deans, M.R., Paul, D.L., Kosaka, K., 2005. Neuronal gap junctions in the mouse main
823 olfactory bulb: Morphological analyses on transgenic mice. Neuroscience 134, 757–769.
824 https://doi.org/10.1016/j.neuroscience.2005.04.057

825 Kosaka, T., Kosaka, K., 2008. Heterogeneity of parvalbumin-containing neurons in the mouse main
826 olfactory bulb, with special reference to short-axon cells and βIV-spectrin positive dendritic
827 segments. Neuroscience Research 60, 56–72. https://doi.org/10.1016/j.neures.2007.09.008

828 Kosaka, T., & Kosaka, K., 2016. Neuronal organization of the main olfactory bulb revisited.
829 Anatomical Science International, 91(2), 115–127. https://doi.org/10.1007/s12565-015-0309-7

830 Lalli, G., 2014. Regulation of neuronal polarity. Experimental Cell Research, Cell polarity 328, 267–
831 275. https://doi.org/10.1016/j.yexcr.2014.07.033

832 Lau, M. Y. H., Gadiwalla, S., Jones, S., & Galliano, E., 2024. Different electrophysiological profiles of
833 genetically labelled dopaminergic neurons in the mouse midbrain and olfactory bulb. The European
834 journal of neuroscience, 59(7), 1480–1499. https://doi.org/10.1111/ejn.16239

835 Li, H., Waites, C.L., Staal, R.G., Dobryy, Y., Park, J., Sulzer, D.L., Edwards, R.H., 2005. Sorting of
836 Vesicular Monoamine Transporter 2 to the Regulated Secretory Pathway Confers the
837 Somatodendritic Exocytosis of Monoamines. Neuron 48, 619–633.
838 https://doi.org/10.1016/j.neuron.2005.09.033

839 Li, Y., Tsien, R.W., 2012. pHTomato, a red, genetically encoded indicator that enables multiplex
840 interrogation of synaptic activity. Nature Neuroscience 15, 1047–1053.
841 https://doi.org/10.1038/nn.3126

842 Liberia, T., Blasco-Ibáñez, J.M., Nácher, J., Varea, E., Zwafink, V., Crespo, C., 2012. Characterization of
843 a population of tyrosine hydroxylase-containing interneurons in the external plexiform layer of the
844 rat olfactory bulb. Neuroscience 217, 140–153. https://doi.org/10.1016/j.neuroscience.2012.05.007

845 Liu, R.-J., Lambe, E.K., Aghajanian, G.K., 2005. Somatodendritic autoreceptor regulation of
846 serotonergic neurons: dependence on L-tryptophan and tryptophan hydroxylase-activating kinases.
847 European Journal of Neuroscience 21, 945–958. https://doi.org/10.1111/j.1460-9568.2005.03930.x

848 Liu, S., 2020. Dopaminergic Modulation of Glomerular Circuits in the Mouse Olfactory Bulb. Frontiers
849 in Cellular Neuroscience 14. https://doi.org/10.3389/fncel.2020.00172

850 Liu, S., Plachez, C., Shao, Z., Puche, A., Shipley, M.T., 2013. Olfactory Bulb Short Axon Cell Release of
851 GABA and Dopamine Produces a Temporally Biphasic Inhibition–Excitation Response in External
852 Tufted Cells. Journal of Neuroscience 33, 2916–2926. https://doi.org/10.1523/JNEUROSCI.3607-
853 12.2013

854 Lyons-Warren, A.M., Tantry, E.K., Moss, E.H., Kochukov, M.Y., Belfort, B.D.W., Ortiz-Guzman, J.,
855 Freyberg, Z., Arenkiel, B.R., 2023. Co-transmitting interneurons in the mouse olfactory bulb regulate
856 olfactory detection and discrimination. Cell Reports 42, 113471.
857 https://doi.org/10.1016/j.celrep.2023.113471

858 Madisen, L., Zwingman, T.A., Sunkin, S.M., Oh, S.W., Zariwala, H.A., Gu, H., Ng, L.L., Palmiter, R.D.,
859 Hawrylycz, M.J., Jones, A.R., Lein, E.S., Zeng, H., 2010. A robust and high-throughput Cre reporting
860 and characterization system for the whole mouse brain. Nature Neuroscience 13, 133–140.
861 https://doi.org/10.1038/nn.2467

862 Maher, B.J., Westbrook, G.L., 2008. Co-Transmission of Dopamine and GABA in Periglomerular Cells.
863 Journal of Neurophysiology 99, 1559–1564. https://doi.org/10.1152/jn.00636.2007

864 Marshak, D.W., 2016. A tale of two neurotransmitters. Visual Neuroscience 33, E017.
865 https://doi.org/10.1017/S0952523816000146

866 McGann, J.P., 2013. Presynaptic Inhibition of Olfactory Sensory Neurons: New Mechanisms and
867 Potential Functions. Chemical Senses 38, 459–474. https://doi.org/10.1093/chemse/bjt018

868 McGann, J.P., Pírez, N., Gainey, M.A., Muratore, C., Elias, A.S., Wachowiak, M., 2005. Odorant
869 Representations Are Modulated by Intra- but Not Interglomerular Presynaptic Inhibition of Olfactory
870 Sensory Neurons. Neuron 48, 1039–1053. https://doi.org/10.1016/j.neuron.2005.10.031

871 McLean, J. H., & Shipley, M. T., 1988. Postmitotic, postmigrational expression of tyrosine hydroxylase
872 in olfactory bulb dopaminergic neurons. Journal of Neuroscience, 8(10), 3658–3669.
873 https://doi.org/10.1523/JNEUROSCI.08-10-03658.1988

874 Murphy, G.J., Darcy, D.P., Isaacson, J.S., 2005. Intraglomerular inhibition: signaling mechanisms of an
875 olfactory microcircuit. Nature Neuroscience 8, 354–364. https://doi.org/10.1038/nn1403

876 Murthy, V.N., 2011. Olfactory Maps in the Brain. Annual Reviews in Neuroscience 34, 233–258.
877 https://doi.org/10.1146/annurev-neuro-061010-113738

878 Nunes, D., Kuner, T., 2018. Axonal sodium channel NaV1.2 drives granule cell dendritic GABA release
879 and rapid odor discrimination. PLOS Biology 16, e2003816.
880 https://doi.org/10.1371/journal.pbio.2003816

881 Panzanelli, P., Fritschy, J. m., Yanagawa, Y., Obata, K., & Sassoè-Pognetto, M., 2007. GABAergic
882 phenotype of periglomerular cells in the rodent olfactory bulb. Journal of Comparative Neurology,
883 502(6), 990–1002. https://doi.org/10.1002/cne.21356

884 Parrish-Aungst, S., Shipley, M. t., Erdelyi, F., Szabo, G., & Puche, A. c., 2007. Quantitative analysis of
885 neuronal diversity in the mouse olfactory bulb. Journal of Comparative Neurology, 501(6), 825–836.
886 https://doi.org/10.1002/cne.21205

887 Parsa, P.V., D'Souza, R.D., Vijayaraghavan, S., 2015. Signaling between periglomerular cells reveals a
888 bimodal role for GABA in modulating glomerular microcircuitry in the olfactory bulb. Proceedings of
889 the National Academy of Sciences 112, 9478–9483. https://doi.org/10.1073/pnas.1424406112

890 Pignatelli, A., & Belluzzi, O., 2017. Dopaminergic Neurones in the Main Olfactory Bulb: An Overview
891 from an Electrophysiological Perspective. Frontiers in Neuroanatomy, 11.
892 https://doi.org/10.3389/fnana.2017.00007

893 Pinching, A.J., Powell, T.P.S., 1971. The neuron types of the glomerular layer of the olfactory bulb.
894 Journal of Cell Science 9, 305–345. https://doi.org/10.1242/jcs.9.2.305

895 Pucak, M.L., Grace, A.A., 1994. Regulation of substantia nigra dopamine neurons. Critical Reviews in
896 Neurobiology 9, 67–89.

897 Rasband, M.N., 2010. The axon initial segment and the maintenance of neuronal polarity. Nature
898 Reviews Neuroscience 11, 552–562. https://doi.org/10.1038/nrn2852

899 Risher, M.-L., Sexton, H.G., Risher, W.C., Wilson, W.A., Fleming, R.L., Madison, R.D., Moore, S.D.,
900 Eroglu, C., Swartzwelder, H.S., 2015. Adolescent Intermittent Alcohol Exposure: Dysregulation of
901 Thrombospondins and Synapse Formation are Associated with Decreased Neuronal Density in the
902 Adult Hippocampus. Alcoholism: Clinical and Experimental Research 39, 2403–2413.
903 https://doi.org/10.1111/acer.12913

904 Rosser, A. E., Hökfelt, T., & Goldstein, M., 1986. LHRH and catecholamine neuronal systems in the
905 olfactory bulb of the mouse. Journal of Comparative Neurology, 250(3), 352–363.
906 https://doi.org/10.1002/cne.902500308

907 Schindelin, J., Arganda-Carreras, I., Frise, E., Kaynig, V., Longair, M., Pietzsch, T., Preibisch, S.,
908 Rueden, C., Saalfeld, S., Schmid, B., Tinevez, J. Y., White, D. J., Hartenstein, V., Eliceiri, K., Tomancak,
909 P., & Cardona, A., 2012. Fiji: an open-source platform for biological-image analysis. Nature Methods,
910 9(7), 676–682. https://doi.org/10.1038/nmeth.2019

Schoppa, N.E., Urban, N.N., 2003. Dendritic processing within olfactory bulb circuits. Trends in Neurosciences 26, 501–506. https://doi.org/10.1016/S0166-2236(03)00228-5

Schoppa, N.E., Westbrook, G.L., 2002. AMPA autoreceptors drive correlated spiking in olfactory bulb glomeruli. Nature Neuroscience 5, 1194–1202. https://doi.org/10.1038/nn953

Shao, Z., Puche, A.C., Liu, S., Shipley, M.T., 2012. Intraglomerular inhibition shapes the strength and temporal structure of glomerular output. Journal of Neurophysiology 108, 782–793. https://doi.org/10.1152/jn.00119.2012

Smith, T.C., Jahr, C.E., 2002. Self-inhibition of olfactory bulb neurons. Nature Neuroscience 5, 760–766. https://doi.org/10.1038/nn882

Soucy, E.R., Albeanu, D.F., Fantana, A.L., Murthy, V.N., Meister, M., 2009. Precision and diversity in an odor map on the olfactory bulb. Nature Neuroscience 12, 210–220. https://doi.org/10.1038/nn.2262

Thévenaz, P., Unser, M., 2007. User-friendly semiautomated assembly of accurate image mosaics in microscopy. Microscopy Research and Technique 70, 135–146. https://doi.org/10.1002/jemt.20393

Tomassy, G.S., Berger, D.R., Chen, H.-H., Kasthuri, N., Hayworth, K.J., Vercelli, A., Seung, H.S., Lichtman, J.W., Arlotta, P., 2014. Distinct Profiles of Myelin Distribution Along Single Axons of Pyramidal Neurons in the Neocortex. Science 344, 319–324. https://doi.org/10.1126/science.1249766

Tufo, C., Poopalasundaram, S., Dorrego-Rivas, A., Ford, M.C., Graham, A., Grubb, M.S., 2022. Development of the mammalian main olfactory bulb. Development 149, dev200210. https://doi.org/10.1242/dev.200210

Tufo, C., Cheah, M., Lipovsek, M., Byrne, D.J., Kothandapani, K., Browne, L.P., Grubb, M.S., 2025. Functional maturation and experience-dependent plasticity in adult-born olfactory bulb dopaminergic neurons. European Journal of Neuroscience 62(1), e70188. https://doi.org/10.1111/ejn.70188

Uchida, N., Takahashi, Y.K., Tanifuji, M., Mori, K., 2000. Odor maps in the mammalian olfactory bulb: domain organization and odorant structural features. Nature Neuroscience 3, 1035–1043. https://doi.org/10.1038/79857

Urban, N.N., 2002. Lateral inhibition in the olfactory bulb and in olfaction. Physiology & Behavior 77, 607–612. https://doi.org/10.1016/S0031-9384(02)00895-8

Vaaga, C.E., Yorgason, J.T., Williams, J.T., Westbrook, G.L., 2017. Presynaptic gain control by endogenous cotransmission of dopamine and GABA in the olfactory bulb. Journal of Neurophysiology 117, 1163–1170. https://doi.org/10.1152/jn.00694.2016

van Beuningen, S.F.B., Will, L., Harterink, M., Chazeau, A., van Battum, E.Y., Frias, C.P., Franker, M.A.M., Katrukha, E.A., Stucchi, R., Vocking, K., Antunes, A.T., Slenders, L., Doulkeridou, S., Sillevis Smitt, P., Altelaar, A.F.M., Post, J.A., Akhmanova, A., Pasterkamp, R.J., Kapitein, L.C., de Graaff, E., Hoogenraad, C.C., 2015. TRIM46 Controls Neuronal Polarity and Axon Specification by Driving the Formation of Parallel Microtubule Arrays. Neuron 88, 1208–1226. https://doi.org/10.1016/j.neuron.2015.11.012

Wachowiak, M., Cohen, L.B., 1999. Presynaptic Inhibition of Primary Olfactory Afferents Mediated by Different Mechanisms in Lobster and Turtle. Journal of Neuroscience 19, 8808–8817. https://doi.org/10.1523/JNEUROSCI.19-20-08808.1999

Whitesell, J.D., Sorensen, K.A., Jarvie, B.C., Hentges, S.T., Schoppa, N.E., 2013. Interglomerular Lateral Inhibition Targeted on External Tufted Cells in the Olfactory Bulb. Journal of Neuroscience 33, 1552–1563. https://doi.org/10.1523/JNEUROSCI.3410-12.2013

Wu, C., Ivanova, E., Cui, J., Lu, Q., Pan, Z.-H., 2011. Action Potential Generation at an Axon Initial Segment-Like Process in the Axonless Retinal AII Amacrine Cell. Journal of Neuroscience 31, 14654–14659. https://doi.org/10.1523/JNEUROSCI.1861-11.2011

Zak, J.D., Schoppa, N.E., 2022. Neurotransmitter regulation rather than cell-intrinsic properties shapes the high-pass filtering properties of olfactory bulb glomeruli. The Journal of Physiology 600, 393–417. https://doi.org/10.1113/JP282374

Zhang, S., Qi, J., Li, X., Wang, H.-L., Britt, J.P., Hoffman, A.F., Bonci, A., Lupica, C.R., Morales, M., 2015. Dopaminergic and glutamatergic microdomains in a subset of rodent mesoaccumbens axons. Nature Neuroscience 18, 386–392. https://doi.org/10.1038/nn.3945

Zilberter, Y., Kaiser, K.M.M., Sakmann, B., 1999. Dendritic GABA Release Depresses Excitatory Transmission between Layer 2/3 Pyramidal and Bitufted Neurons in Rat Neocortex. Neuron 24, 979–988. https://doi.org/10.1016/S0896-6273(00)81044-2

Supplementary Figure 1

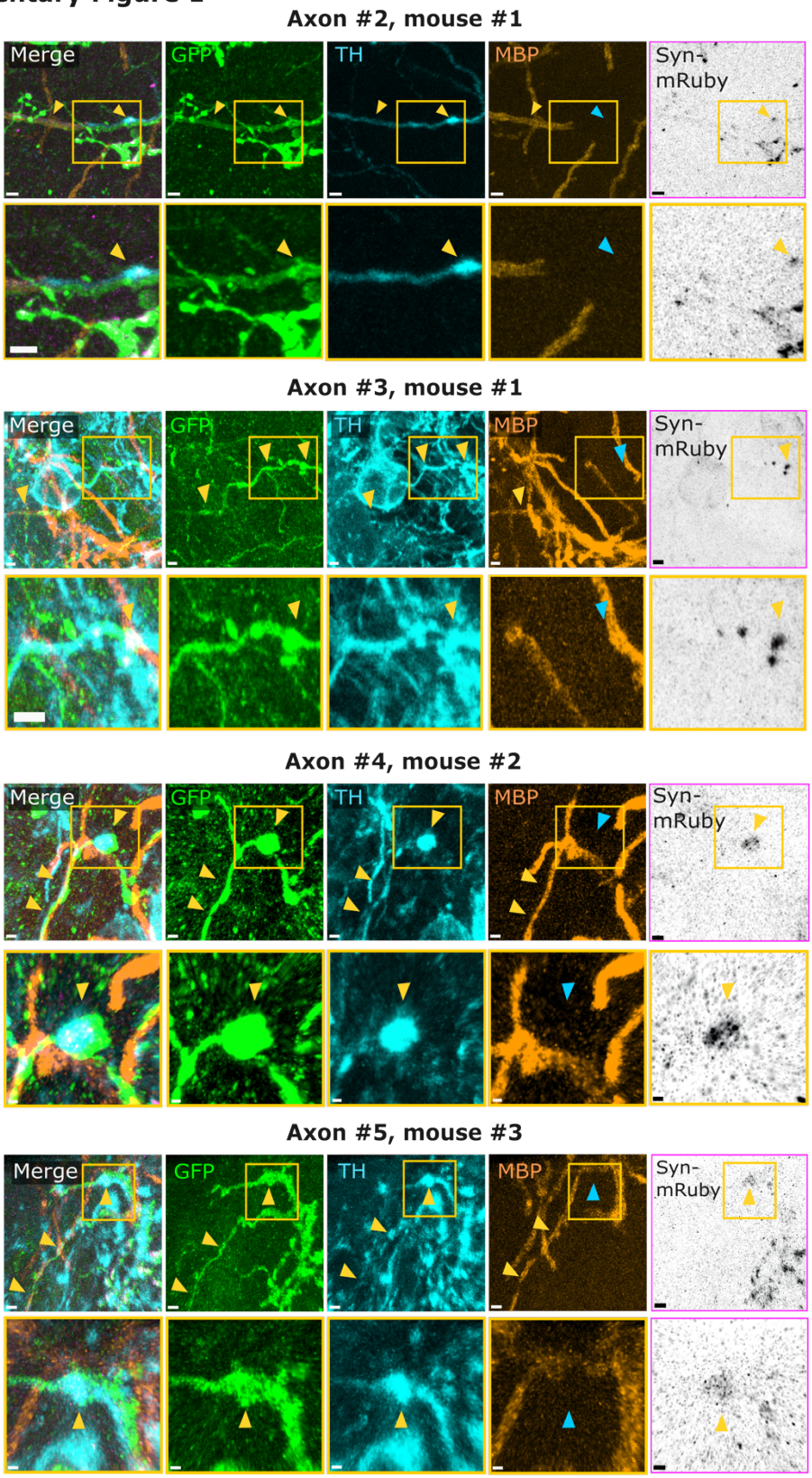

Supplementary figure 1 (related to Figure 3). Example confocal images of dopaminergic axons from different mice. Neurons are stained with GFP (green), TH (blue), MBP (orange), and Synaptophysin-mRuby (black). Yellow arrows show co-localisation between the different channels; blue arrows show lack of co-localisation. Yellow inset highlights the location of the presynaptic bouton. Images at the bottom are zoomed-in snapshots

978 from the images at the top, and arrows point at the synaptic puncta. Scalebars for axon #2, 2 μm and 1 μm; for
979 axon #3, 10 μm and 5 μm; for axon #4, 1 μm and 0.5 μm; and for axon #5, 2 μm and 1 μm.

Supplementary Figure 2

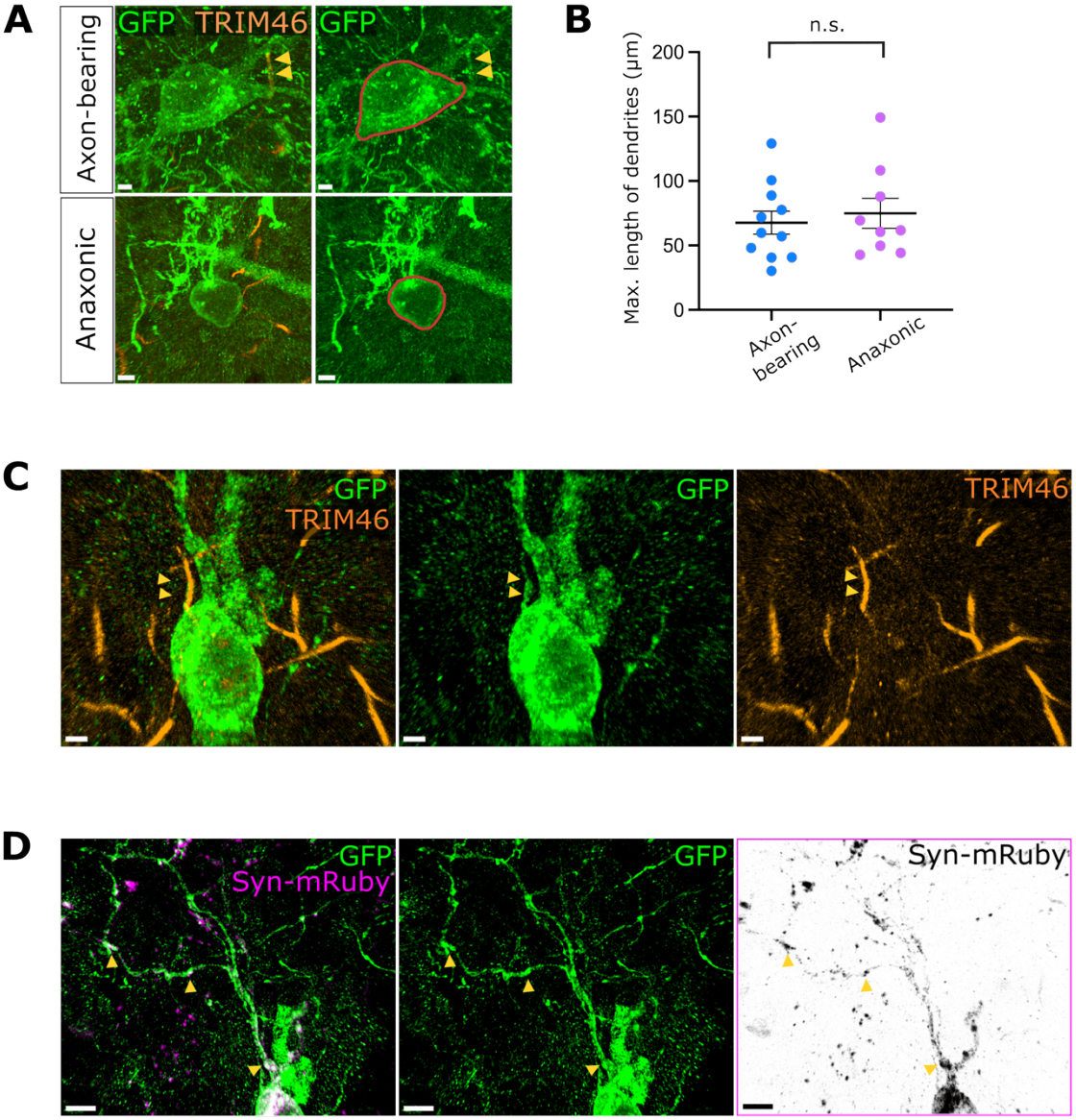

980

981 **Supplementary figure 2 (related to Figure 3). (A).** Example confocal images showing soma size measurements
982 in axon-bearing and anaxonic DA neurons**.** Axon-bearing (top) and anaxonic (bottom) cells labelled with GFP
983 (green) and TRIM46 (orange). Yellow arrowheads point to the TRIM46-positive segment, indicating that the
984 neuron has an axon. Red lines highlight the soma of the two neurons. Scalebars, 3 μm. **(B)** Maximum length of
985 traced dendrites for axon-bearing (blue) and anaxonic (magenta) DA neurons. Each dot represents one cell,
986 lines show mean ± SEM, n = 11 axon-bearing neurons and n = 9 anaxonic cells from N = 4 mice, Welch's t-test,
987 p = 0.63, n.s. = non-significant. **(C, D)** Dendritic mRuby puncta in a strongly over-expressing axon-bearing
988 neuron **(C)** Example confocal image with GFP (green) and TRIM46 (orange) labelling, revealing the axon-
989 bearing identity of the neuron. Yellow arrowheads point to the GFP+/TRIM46+ co-localised zone. Scalebars, 2
990 mm. **(D)** Example confocal images showing synaptophysin-mRuby label (magenta, black) in the dendrites of
991 the axon-bearing neuron from (C) (green). The levels of synaptophysin-mRuby look dramatically higher and

992 with a less defined puncta profile than in all anaxonic DA cells – note levels of somatic expression compared to
993 Figure 2B. Yellow arrowheads point to examples of detected puncta. Scalebars, 5 μm.

Supplementary Figure 3

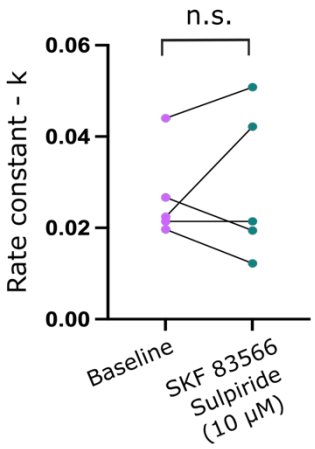

994 **Supplementary figure 3 (related to Figure 4).** Comparison of the decay constant k of the auto-evoked
995 inhibition response before (magenta) and after (green) the application of D1 and D2 receptor antagonists.
996 Each dot represents one cell, n = 6 cells from N = 4 mice, Wilcoxon signed-rank test, p = 0.84, n.s. = non-
997 significant.

Supplementary Figure 4

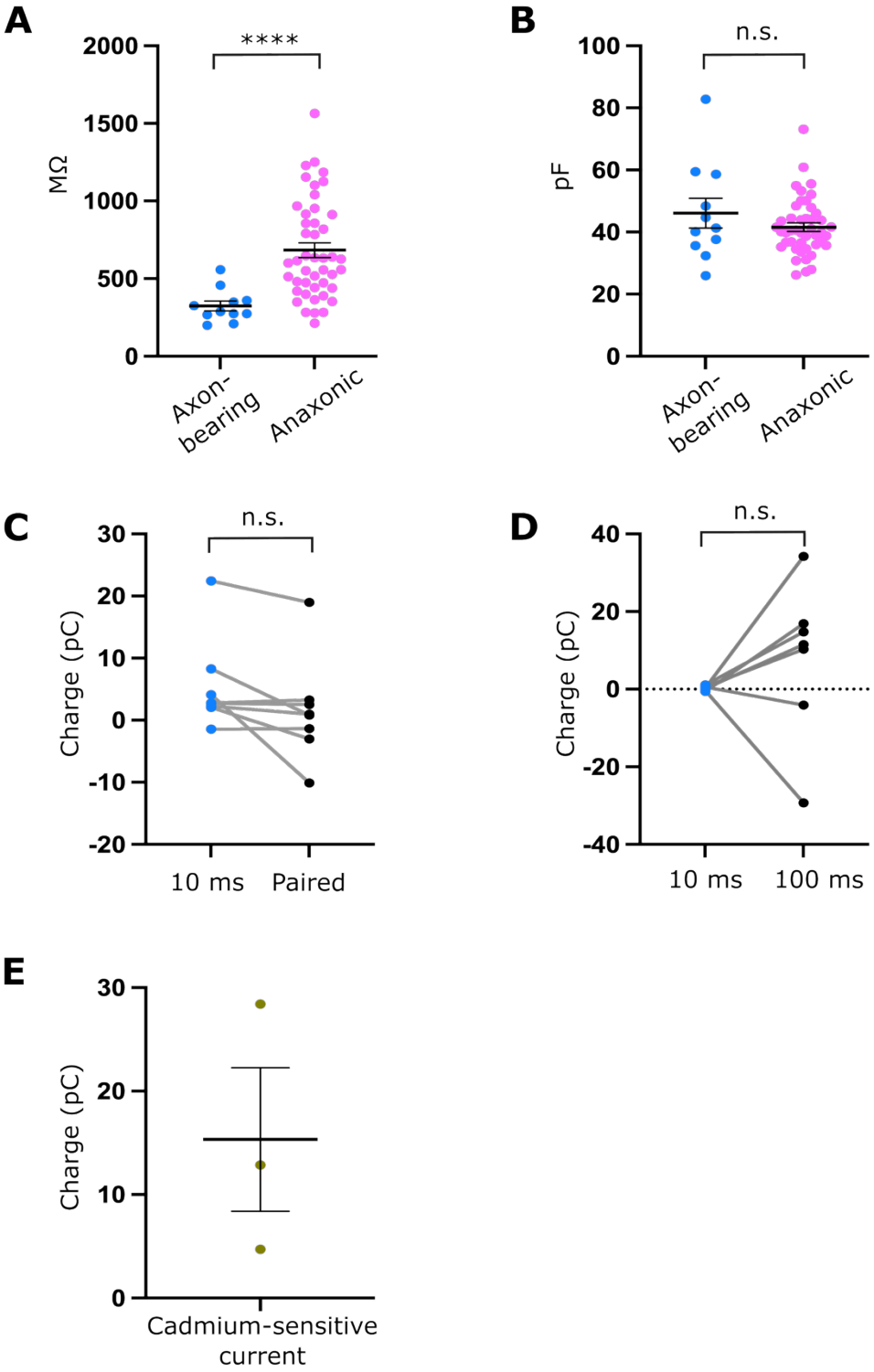

Supplementary figure 4 (related to Figure 5). (A) Input resistance in axon-bearing (blue) and anaxonic (magenta) DA neurons. Each dot represents one cell, horizontal lines show the mean ± SEM, n = 11 axon-bearing neurons and n = 45 anaxonic cells from N = 32 mice, ****, p<0.0001, Mann-Whitney test. **(B)** Membrane capacitance in axon-bearing (blue) and anaxonic (magenta) DA neurons. All conventions as in (A), n=11 axon-bearing neurons and n=45 anaxonic cells from N = 32 mice, Mann-Whitney test, n.s. = non-

significant. **(C)** Comparison of AEI charge for single (blue) and paired response (black) in axon-bearing cells. Each dot represents one cell, grey lines connect measurements from the same cell; n = 8 cells from N = 7 mice; Wilcoxon matched-pairs signed rank test, p = 0.06, n.s. = non-significant. **(D)** Comparison of the auto-evoked inhibition charge in axon-bearing cells following either a 10 ms or 100 ms depolarisation step. All conventions as in (C), n = 7 cells from N = 6 mice; Wilcoxon matched pairs signed rank test, p = 0.30, n.s. = non-significant. **(E)** Cadmium-sensitive current in axon-bearing DA neurons, n = 3 cells from N = 3 mice, all conventions as in (A).

Supplementary Figure 5

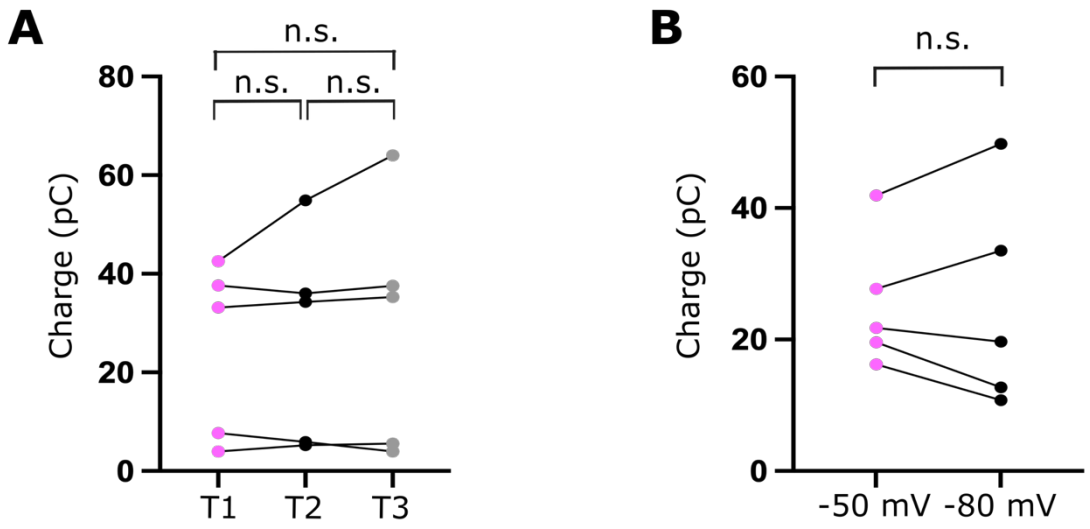

Supplementary figure 5 (related to the auto-evoked inhibition recordings section of Materials and Methods). (A) Comparison of the analysed auto-evoked inhibition charge after three repeats of the auto-evoked inhibition protocol. Circles represent individual cells, lines connect data from the same neuron; n = 5 cells from N = 4 mice; repeated measures one-way ANOVA, p = 0.44, n.s. = non-significant. **(B)** Comparison of the auto-evoked inhibition charge from a holding potential of either -50 mV or -80 mV. All conventions as in (A), n = 5 cells from N = 3 mice, paired t-test, p = 0.96, n.s. = non-significant.